Highlights

A software tool for the estimation of uncertainties and spectral error correlation in Sentinel-2 Level-2A data products

Javier Gorroño, Luis Guanter, Lukas Valentin Graf, Ferran Gascon

- Development of a software tool to calculate uncertainty and spectral error correlation for Sentinel 2 L2A products.
- Impact of Sentinel 2 L2A uncertainty and spectral error correlation in the uncertainty propagation of phenology metrics.

A software tool for the estimation of uncertainties and spectral error correlation in Sentinel-2 Level-2A data products

Javier Gorroño[a,*], Luis Guanter[a,b], Lukas Valentin Graf[c,d], Ferran Gascon[e]

[a] *Research Institute of Water and Environmental Engineering (IIAMA), Universitat Politècnica de València, Camí de Vera s/n, València, 46022, , Spain*
[b] *Environmental Defense Fund, Reguliersgracht 79, Amsterdam, 1017 LN, , The Netherlands*
[c] *Crop Science, Institute of Agricultural Science, ETH Zurich, Universitaetstrasse 2, Zurich, 8092, , Switzerland*
[d] *Earth Observation of Agroecosystems Team, Division Agroecology and Environment, Agroscope, Reckenholzstrasse 191, Zurich, 8046, , Switzerland*
[e] *European Space Agency, Via Galileo Galilei, Frascati, 00044, , Italy*

Abstract

The Copernicus Sentinel-2 (S2) satellite mission acquires high spatial resolution optical imagery over land and coastal areas. Delivering uncertainty estimates and spectral error correlation alongside S2 data products facilitates the constrain of retrieval algorithms, propagate further downstream the retrieval uncertainty, and finally make informed decisions to end-users. This study presents a software (available at Gorroño (2023)) that generates uncertainty estimates and spectral error correlation associated to the S2 L2A data products (i.e. surface reflectance). The uncertainty considers both the Level-1 (L1) uncertainty estimates for top-of-atmosphere (TOA) reflectance factor and the atmospheric correction. The propagation is performed with a Multivariate MonteCarlo model that effectively accounts for the spectral error correlation between S2 L2A bands. The uncertainty analysis involves the propagation of the L1C TOA reflectance factor through the atmospheric correction using LibRadtran. This propagation accounts for input uncertainty such as L1 TOA reflectance, aerosol optical thickness (AOT) or adjacency

---

[*] Corresponding author.
Email address: `jagorvie@upv.es` (Javier Gorroño)

Preprint submitted to ISPRS Journal Of Photogrammetry And Remote Sensing June 16, 2023

correction. On the top of this propagation we also model the contributions from the Lambertain assumption of the correction model and the estimated accuracy of the LibRadTran software. We show results for surface reflectance uncertainty at two different sites. The examples over the Amazon forest and Libya4 desert site illustrate the large variations of the uncertainty levels and spectral error correlation depending on the scene. Furthermore, we include an example on the propagation of surface reflectance uncertainty to spectral vegetation indices. The propagation over vegetation metrics indicates a strong dependence of the error covariance matrix with the phenological cycle and exemplifies how critical is that S2 L2A products include both uncertainty and spectral error correlation since they are effectively the input to many different land surface parameters. Its implementation as an operational per-pixel processing and dissemination of both the uncertainty and spectral error correlation becomes challenging. However, exploring cloud computing and machine learning techniques could become an adequate pathway to minimise these challenges.

Keywords: Copernicus, uncertainty, spectral error correlation, surface reflectance, Level-2A

---

1. Introduction

Earth Observation (EO) via satellite remote sensing has exponentially increased in terms of data and applications in the last decade. It is nowadays an important source of information about the Earth system with areas of application that include, for example, climate studies or agriculture monitoring. The increased complexity of these applications and the growing number of data products has triggered the need to include a quality indicator that describes the compatibility between satellite products and the suitability for particular applications. Some initiatives such as Quality Assurance framework for Earth Observation (QA4EO), established and endorsed by Committee on Earth Observation Satellites (CEOS), actively work on a high level framework that becomes the basis of a rigorous quality assessment for EO satellite missions (Team, 2010).

Recent efforts by the community have made possible for some satellite missions to offer operational Level-1 (L1) uncertainty estimates at top-of-atmosphere (TOA) radiance/reflectance factor. The Moderate Resolution Imaging Spectroradiometer (MODIS) instrument on-board the Aqua and

Terra missions produces uncertainty estimates associated with the L1B product (Esposito et al., 2004; Xiong et al., 2017) as well as the Copernicus Sentinel-2 (S2) satellite mission does it for the L1C products through the L1 Radiometric Uncertainty Tool (L1-RUT) (Gorroño et al., 2017).

The Copernicus S2 satellite mission currently comprises two satellites (S2A and S2B) and provides continuous monitoring of terrestrial surfaces and coastal waters at a global scale with better than a 5-day revisit (Drusch et al., 2012). The main payload on-board is the Multi-Spectral Instrument (MSI) with 13 spectral bands in the visible and near-infrared (VNIR) and the shortwave infrared (SWIR) at spatial resolutions of 10, 20 or 60 m. The S2 Level-2A (L2A) data product is generated after the atmospheric correction of the L1C observations. The L2A product data approximates to the directional-hemispherical reflectance at a surface (or top of canopy level) (Nicodemus et al., 1977; Schaepman-Strub et al., 2006). From here on, we refer as *surface reflectance* for simplification. The L2A data products are delivered in a set of ortho-images (in UTM/WGS84 projection) of about 100 ×100 km (Gascon et al., 2017). The L2A product represents the most advanced data offered to the users and it is the input to many different land surface parameters. Including uncertainty information associated to these data products would be highly relevant to improve retrieval algorithms or provide uncertainty information in different end-user applications such as phenology metrics.

Several efforts have been made in bringing uncertainties into land surface parameter retrievals. For example, the work in Kaminski et al. (2017) describes the Joint Research Centre - Two Stream Inversion Package (JRC-TIP) which retrieves land surface parameters along with uncertainty and error correlation estimates. The observation space is defined by the MODIS collection V005 (MCD43B3) broadband white-sky albedo products. Although these data products include a quality flag with a broad uncertainty estimation, there is no spectral error correlation information and, therefore, the covariance matrix is set to zeros for all values but the diagonal. Another example can be found in García-Haro et al. (2018) where an uncertainty estimate is associated to the leaf area index (LAI), the fractional vegetation cover (FVC), and the fraction of absorbed photosynthetically active radiation (FAPAR). The uncertainty is quantified as a combination of the predictive standard deviation and the propagation of the Bi-Directional Reflectance Function (BRDF) model uncertainty. Similarly to the previous case in Kaminski et al. (2017), the input BRDF uncertainty is modelled as independent Gaussian variables.

Although these examples represent a clear advance in providing uncertainty estimates in a rigorous manner for land surface parameters, the reality is that limited detailed uncertainty and covariance information in the observations hinders further efforts. Indeed, it illustrates how the absence of operational uncertainty estimates for surface reflectance products, limits its propagation to further processing levels mainly in land retrieval methods. Thus, the main objective of this project is the generation of uncertainty and spectral error correlation information (i.e. full covariance matrix) associated to the S2 L2A data products.

The impact of this novel information is not only addressed to land surface parameters. It is also expected (but not limited) to:

- *Derive new and better-quality metrics for end-user applications.* For example, in the field of agricultural monitoring, the study in Graf et al. (2023) explores an uncertainty propagation framework for the S2 data products that translates the L1C and L2A uncertainty into an uncertainty in the vegetation parameters and ultimately into land surface phenological metrics.

- *Constrain measurement space in retrieval methods.* In a Bayesian framework the actual mapping of predictions is constrained by the observations and prior covariance matrices. The accurate definition of these uncertainty levels and their spectral error correlation can produce significant benefits on the vegetation parameters retrieval.

- *Improve the compliance and quality information of L2A data products.* Reliable information of quantitative EO data products are crucial for decision making processes such as regulatory initiatives or contractual negotiations for the operational exploitation of EO data. (Widlowski, 2015).

The paper briefly defines the atmospheric correction of the L2A data products in subsection 2.1, then it describes each one of the considered uncertainty contributions in subsection 2.2 and the aforementioned uncertainty methodologies. The multivariate MCM approach and a brief description of the software and implementation is synthesised in subsection 2.3. An adapted version of the GUM analytical approach has been implemented for testing purposes and is described in subsection 2.4. The results in section 3 include examples for a scene of the Amazon forest and another in the Sahara desert in subsection 3.1. The difference between a GUM analytical approach and a multivariate method are presented in subsection 3.2. Finally, subsection 3.3 presents a case study where both the uncertainty and spectral error correlation estimates are propagated into vegetation indexes.

2. Methodology

2.1. Atmospheric correction in Sen2Cor

The current L2A operational products delivered by ESA are generated with Sen2Cor both from the user side and from the ground segment (Louis, 2021). Sen2Cor performs a pre-processing of L1C reflectance including a scene classification, an atmospheric correction and a conversion into surface reflectance orthoimages that define the main content of the L2A product. In addition, the algorithm also delivers an Aerosol Optical Thickness (AOT) map, a Water Vapour (WV) map and a Scene Classification map.

The atmospheric correction is based on precompiled Look-Up tables (LUTs) that contain the main atmospheric functions for a large homogeneous Lambertian surface generated with LibRadtran radiative transfer (Louis, 2021).

The input for the Sen2Cor atmosperic correction is the TOA radiance L_{TOA} that is converted from the L1C TOA reflectance ρ_{TOA} as follows:

$$L_{\text{TOA}}(\lambda) = \frac{E_S \cdot \cos\Theta_s}{\pi \cdot d^2} \rho_{\text{TOA}}(\lambda) \tag{1}$$

where Θ_s refers to the sun zenith angle (SZA), d to the Sun-Earth distance in astronomical units and E_S refers to the sun irradiance that for the S2 data products is modelled based on Thuillier model (Thuillier et al., 2003).

The atmospheric correction over a flat terrain neglects, in a first step, the influence of the neighbourhood (adjacency effect) and the surface reflectance is obtained as:

$$\rho^I(i,j) = \frac{\pi \cdot (L_{\text{TOA}}(i,j) - L_p)}{\tau \cdot E_g} \tag{2}$$

where τ is the ground-to-sensor transmittance, L_p refers to the path radiance and E_g to the downwelling irradiance on the ground.

In a second step, the initial surface reflectance is corrected for the adjacency effect following the expression:

$$\rho^{II}(i,j) = \rho^I(i,j) + q \cdot (\overline{\rho^I} - \rho(i,j)) \tag{3}$$

where $\overline{\rho^I}$ represents a mean reflectance over a predefined area and $q = \frac{\tau_{diff}}{\tau_{dir}}$ represents the strength of the adjacency effect. It is the ratio of the diffuse to direct ground-to-sensor transmittance.

The Sen2Cor does not include a further step but here we include a further correction as in ATCOR software that includes the spherical albedo effect s on the global flux that is initially set to a default values and needs to be adapted to the scene specific level (Richter and Schläpfer, 2019). The correction is written as:

$$\rho^{III}(i,j) = \rho^{II}(i,j) \cdot [1 - (\overline{\rho^I} - \rho_r) \cdot s] \tag{4}$$

where ρ_r is the reference reflectance set at a value of 0.15.

2.2. L2A product uncertainty contributions

2.2.1. L1C uncertainty

The L1C uncertainty is described in Gorroño et al. (2017) and includes several contributions such as the diffuser calibration uncertainty or the dark signal stability.

The original code (available online at `https://github.com/senbox-org/snap-rut`) has been converted into a sampling scheme based on a multivariate MCM. The code considers the spectral error correlation between the considered L1C uncertainty contributions based on the description in Gorroño et al. (2018). The result is a set of samples for each band that represent the error distribution at L1C reflectance and inherently include the spectral error correlation between them.

The irradiance uncertainty has been also included in the code but only for test purposes. This contribution is cancelled out when considering TOA reflectance uncertainty (Gorroño et al., 2017). However, the data in Sen2Cor is converted back into TOA radiance (see Equation 1) and, although it is cancelled out again during the atmospheric correction, it is possible that a small effect remains and/or other effects (e.g. rounding) need to be considered. Uncertainty for this contribution has been modelled based on estimates in VNIR from Thuillier et al. (1998) and SWIR from Thuillier et al. (2003). Correlation information has been based on the assumption that the error correlation decreases with the spectral distance.

2.2.2. Uncertainty in atmospheric parameters

The uncertainty on the parameterisation input space is propagated through Libradtran radiative transfer. The selection of a multivariate MCM simplifies the modelling since the spectral error correlation and any ad-hoc internal processing steps are inherently included. At the output, we obtain an error distribution for each one of the functions (e.g. path radiance) needed for the atmospheric correction (see subsection 2.1).

Here we detail each one of the main parameters that are included and how they have been parameterised together with the associated uncertainty estimate:

- **Aerosol Optical Thickness** calculated based on the dark dense vegetation (DDV) algorithm in Kaufman et al. (1997) and AOT meteorological estimates from ECMWF CAMS data as a fallback solution (Louis et al., 2018). The theoretical uncertainty for the former could be calculated from the uncertainty propagation through the band ratios calculated during the process. However, estimates for the model uncertainty (e.g. assumed ratios for the bands) become more challenging. Thus, for this first implementation of the software, the values of uncertainty have been obtained from the original requirement (left term in Equations 5 and 6) and expanded with the systematic error (right term in Equations 5 and 6) found through extensive validation against AERONET stations worldwide (S2 MSI ESL team, 2023).

$$\rho_{AOT}^{DDV} = (0.1 \cdot aot + 0.03) + |-0.56 \cdot aot + 0.07| \tag{5}$$

$$\rho_{AOT}^{CAMS} = (0.1 \cdot aot + 0.03) + |-0.46 \cdot aot + 0.09| \tag{6}$$

- **Water vapour** This is based on the APDA (atmospheric precorrected differential absorption) algorithm (Schläpfer et al., 1998). Same reasoning as for the AOT case applies here and the assigned uncertainty is based again on the requirement values expanded with the systematic error obtained from the AERONET validation as follows:

$$\rho_{WV}^{APDA} = (0.1 \cdot wv + 0.2) + |-0.1 \cdot wv + 0.03| \tag{7}$$

- **Ozone** is set to 3% based on a comparison from total column ozone (TCO) satellite estimations against ECMWF ERA-interim (currently superseded by ECMWF ERA-5) in Dragani (2011).

- **SZA, RAA, VZA** uncertainty assumed negligible compared to other sources of uncertainty (e.g. LUT sampling).

- **CH4, CO2 and altitude** assigned a mean of 1.8ppm, 400ppm and mean-tile value from the metadata respectively. Standard deviation allocations of 0.1ppm, 40ppm and 10% respectively.

2.2.3. Adjacency correction uncertainty

The adjacency effect is produced by radiation coming from neighbourhood pixels and scattered into the line-of-sight of the sensor. The standard adjacency kernel window size is 2 km. The adjacency range is not a critical parameter for most pixels but for areas with a high surface contrast (e.g a lake surrounded by forests) (Louis, 2021).

For this first implementation of the L2A budget, the term $\overline{\rho^I}$ in Equation 3 has been modelled with an uncertainty of 3% and a spectral error correlation based on the spectral distance.

2.2.4. Lambertian assumption error

The retrieval presented in subsection 2.1 assumes a Lambertian surface. However, in a real scenario the target surface is expected to be anisotropic and this results in an error on the estimated surface reflectance. These errors depend on the specific target and spectral band. For example, relative errors due to the Lambertian assumption on the surface reflectance have been calculated as 3–12% in the visible and 0.7–5.0% in the near-infrared in Hu et al. (1999). In another example in Franch et al. (2013), mean errors where 3–7% in the red and 2–5% in the near-infrared (depending on optical depth).

For this implementation, we set an uncertainty of 3% for all bands. It might be slightly optimistic for some visible bands but average case in NIR bands.

2.2.5. LibRadtran uncertainty

This last contribution represents the uncertainty introduced by the radiative transfer itself. Benchmarking of radiative transfer typically relies on the comparison of ideal cases such as monochromatic radiation or Lambertian surface assumptions (Kotchenova et al., 2008). Although this might be a good initial assessment to validate and flag issues between radiative transfer codes, it does not represent real conditions for EO satellite observations.

Recent work in Thompson et al. (2021) considers pseudo-invariant sites to infer uncertainty in radiative transfers with a data-driven method. The study in Govaerts et al. (2022) also presents specific radiative transfer model disagreements over pseudo-calibration sites. This second study provides detailed results for different codes (among them Libradtran) and for the Sentinel 2 satellite mission. This per-band errors are calculated as the maximum disagreements between mean bias errors over a long temporal trend of S2 satellite observation against simulated scenes over the Libya-4 calibration site. Although it covers a single site, they are the most detailed and S2-specific estimates of inherent Libradtran uncertainty and we have included them in the first version of the L2A uncertainty. In the VNIR bands, the estimated errors are from 1-2%. The largest relative error is reported for B11 and B12 at the 2-3% where the REPTRAN model has limited capability to reproduce the varying molecular absorption. The error for B8 is reported above 3% but here we will reduce the error to 1.2% since a large contribution was due to the limited spectral resolution of 6SV (see (Vermote et al., 2006)) that is not present in Libradtran.

2.3. Multivariate Monte Carlo model and software implementation

The most common approach for uncertainty estimation is referred as *Guide to the expression of uncertainty in measurement* (GUM) and involves the analytical calculation of the uncertainty through partial derivatives and correlation coefficient (JCGM, 2008a). This was the case for the S2 L1C uncertainty because the radiometric transformations are largely linear and a normal error distribution can be assumed (Gorroño et al., 2017).

The L2A data products from S2 are generated with Sen2Cor processor (Louis et al., 2016). It is based on the inversion of the atmospheric functions precalculated with Libradtran. In this case, we have no explicit mathematical model of the atmospheric functions, no knowledge of their distribution shape, dependence or linearity of the model. In that scenario, the MonteCarlo Model (MCM) is the selected choice since it can work without an explicit mathematical model and can model the input and output dependence and distribution shape (Cox and Siebert, 2006).

We use Libradtran 2.0.4 to generate the error distribution associated to each one of the atmospheric functions (Emde et al., 2016; Mayer and Kylling, 2005). Then, these functions are used to invert the surface reflectance assuming a uniform lambertian surface. Further corrections of these assumptions (such as adjacency correction) and estimated Libradtran accuracy are included in subsequent processing steps (see subsection 2.1). The output represents an error distribution where the measurand (here the surface reflectance) is contained (JCGM, 2008b).

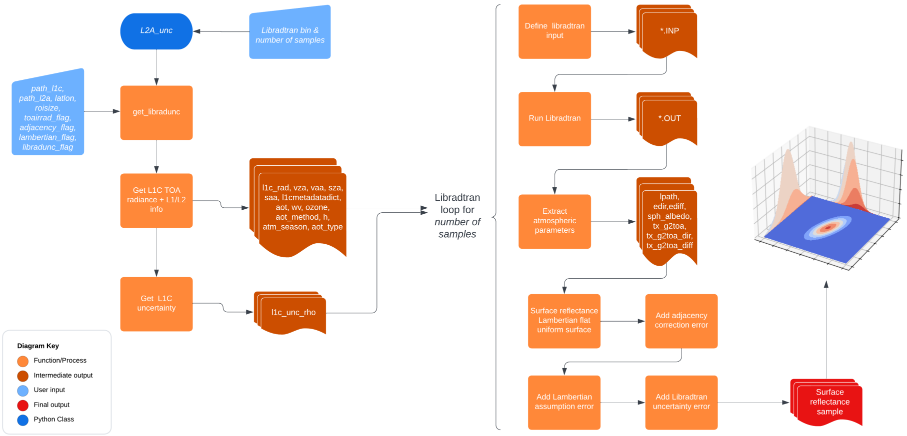

Figure 1: Simplified workflow of the L2A-RUT software.

One important novelty in this approach is that MCM is performed considering the spectral error correlation between the spectral bands. All inputs including L1C data are modelled with a spectral error correlation matrix as well as an uncertainty per band. This results, on the one hand, on a more realistic propagation of uncertainty and, on the other hand, the possibility to offer the user with the full surface reflectance error covariance matrix.

This concept has been implemented in Python code and is accessible in Gorroño (2023). A high-level workflow of the software is depicted in Figure 1.

The software first defines a class named *L2A_unc* and calls a function named *get_libradunc*. This function reads the L1C and L2A data products to extract all possible metadata that defined the Libradtran parameterisation (e.g. estimated value of AOT). Furthermore, it also extracts the L1C reflectance, converts to radiance and estimates an uncertainty based on an adapted version of the L1-RUT (Gorroño et al., 2017, 2018). Once all this information has been obtained, the Libradtran input can be defined, run the radiative transfer code and extract the atmospheric parameters. Finally, the surface reflectance for all bands is calculated and other effects such as adjacency are also included. This process is repeated (defined by the user value) and results in a set of surface reflectance samples that define the surface reflectance distribution for all bands out of which a covariance matrix can be obtained.

From the output, here we offer the uncertainty (k=1) based on the standard deviation of the surface reflectance samples in a normal distribution. If the distribution is considerably asymmetric, the reference JCGM (2008b) recommends the use of the shortest coverage interval that corresponds to a specific coverage factor (e.g. 68.27% for k=1).

The code includes a script *run_L2a_unc.py* that wraps the processing workflow and runs several examples described in Section 3. This code can be found in Appendix D.

The lines 6-23 in this script are the ones of general interest to the user. The `samples` in line 6 must be set to a sufficient number for convergence (1000 is default) whereas the user must define the location of the libradtran binary in line 7. In addition, the user must define the lines 13-16 that contain the L1C and L2A zip product files (`path_L1C` and `path_L2A`), the location in latitude and longitude (tuple `latlon`) and the size of the area in `roisize`. If the user sets `roisize`, the calculation will be generated for a single pixel. Otherwise, it will be performed for the mean value of the rectangular area defined by `roisize`.

All the results will be automatically plotted and stored in the folder *./L2Aunc_results* (you can comment line 23 not to obtain these plots). In any case, all the results will be available in the class variable `lut`. For example `lut.L2Arho` will contain an array with the 12 L2A bands and, for each one of them, the distribution samples.

2.4. GUM analytical approach

In the case of Libradtran, the internal processing steps might present internal binning, ad-hoc processing steps and other post-processing effects such as the convolution with the S2 spectral response that are difficult to model into a single equation. However, we can apply this method for the combination of the atmospheric functions as described in Equations 2, 3 and 4.

The same software as described in subsection 2.3 provides the distribution for each one of the atmospheric functions L_p, E_g, τ and s. Then, a corresponding value of uncertainty can be obtained for each atmospheric function as well as the correlation among them. Furthermore, the sensitivity coefficient for each atmospheric function can be defined from the defined Equations 2, 3 and 4.

In mathematical terms, the GUM analytical framework is defined in matrix form as:

$$U = C \times V \times R \times V^T \times C^T \tag{8}$$

Here C and V are diagonal matrices of the sensitivity coefficients (Jacobian matrix) and uncertainty sources. These uncertainty sources correspond to the atmospheric functions and the L1C radiance. The R matrix is the error correlation matrix between the individual uncertainty sources. On the top of this uncertainty, an effect related to adjacency or other effects might be added.

This analytical and matrix implementation of the uncertainty is an adequate method for the Sen2Cor processor since it minimises the computational requirements on the user side by pre-compiling the uncertainty values for each atmospheric function and correlation. These values could be stored alongside each one of the LUT entries of Sen2Cor. That is for each specific LUT entry in Sen2Cor, we would have the values, uncertainty and error correlation between the atmospheric functions.

We will use this method to compare against the proposed MCM multivariate in subsection 3.2 in order to flag the main strengths and limitations.

3. Results

3.1. MCM results over two scenes

This subsection exemplifies a run and output of the software over two selected sites. These sites are located at latlon = (-6.2869°, -66.8652°) and latlon = (28.55°, 23.39°). They represent a typical Amazon forest and dune area of the Sahara desert. The latter is largely used by the community for radiometric validation of optical instruments onboard satellites (Cosnefroy et al., 1996). The area selected for both sites is 500×500 m^2 since it might become more representative of a typical scene in these sites. Figure 2 contains an RGB image for each one of the sites.

The error distributions for the TOA radiance results in a near-normal distribution as expected (Gorroño et al., 2017). These figures can be found in appendices Appendix A (Figure A.15 for Amazon forest site) and Appendix B (Figure B.23 for Libya-4 desert site) The relative uncertainty varies from 1 to 3% mostly depending on the radiance level. Figures 3 and 4 contain the error distribution for a subset of bands of the surface reflectance that we have obtained by running the multivariate MCM code. All the bands are available in Figures A.14 and B.22.

The relative uncertainty here varies largely depending on the band. The larger relative uncertainty occurs for B9 due to large sensitivity to water vapour. The lowest relative uncertainty (in the range of 3-5%) occur for the rest of the bands in the NIR and SWIR. However, these relative values increase for those bands that are more sensitive to the atmosphere (e.g. B1-B4). In

(a) Amazon forest

(b) Libya4 desert

Figure 2: Selected sites with Figure 2a containing the Amazon forest centered at latlon = (-6.2869°, -66.8652°) and Figure 2b) containing the Libya4 desert at latlon =(28.55°, 23.39°)

those bands, the values can range from 5% to values over the 20%. The error distributions at surface reflectance follow a normal distribution for several bands. This situation does not occur for B9 and B1-B4 of the Amazon forest example. The non-normal distribution of B9 is the result of a large impact of the water vapour absorption and its non-linear response. The slight skewness in the B1-B4 distribution is due to higher impact of the atmosphere.

Figures 3 and 4 are the result of combining the different atmospheric functions and the additional correction steps in Libradtran (see subsection 2.2). Appendix A and Appendix B also include the error distribution for each one of these atmospheric functions for the Amazon forest and Libya-4 desert respectively. The distribution of the different atmospheric functions are close to normal for the desert example, supporting the surface reflectance results. In contrast, the distribution for the different atmospheric functions in the Amazon forest case are highly non-normal and with unexpected response in some of them. The results in the distribution at the surface reflectance only partially reflect a small non-normal response. That is, at some extent, due to the combination of the atmospheric functions that mitigates this non-normal response. For example, the down-welling direct (E_g^{dir}) and diffuse (E_g^{diff}) are completely inversely correlated (i.e. opposite distribution shapes) as summarised in Figure A.21.

In addition to the information of the specific per-band uncertainty, the software also generates the error correlation matrix between the S2 bands. The result for each one of the examples is given in Figure 5.

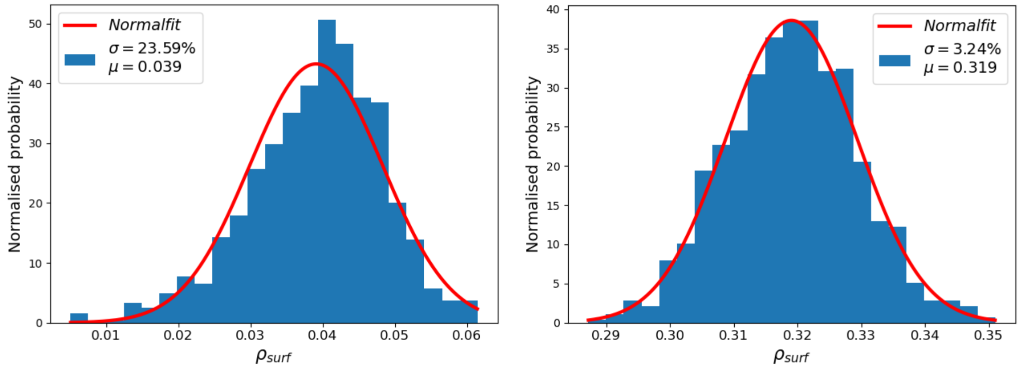

(a) B1

(b) B8

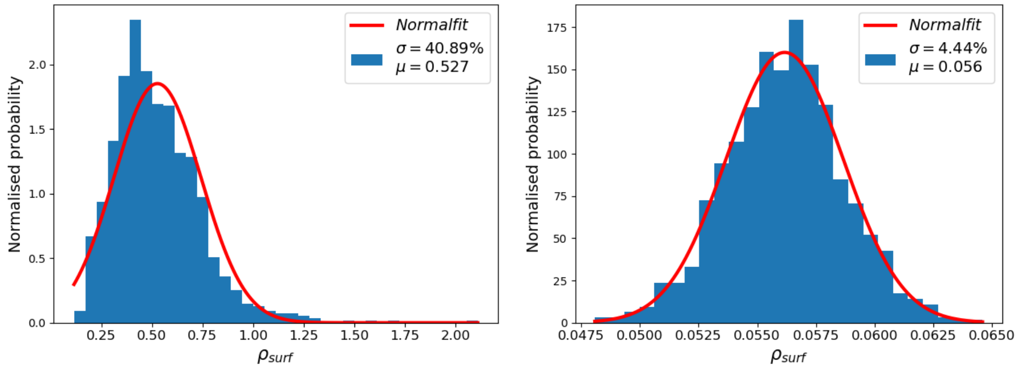

(c) B9

(d) B12

Figure 3: Surface reflectance for a set of bands in the Amazon forest obtained with the L2A-RUT code.

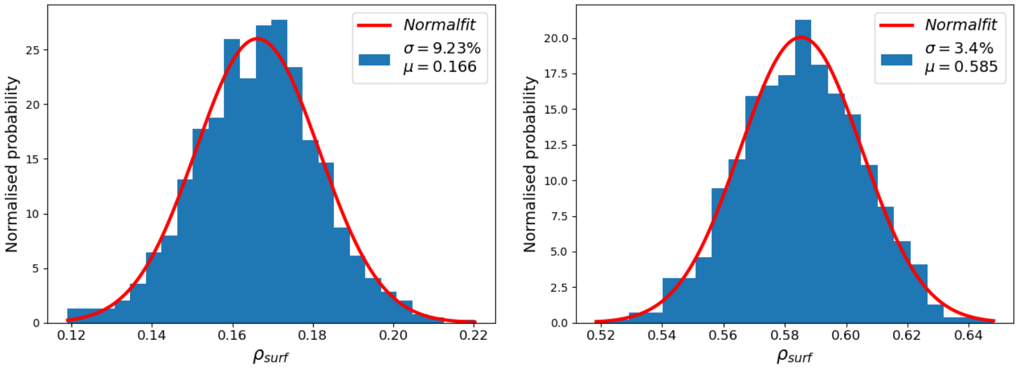

(a) B1 (b) B8

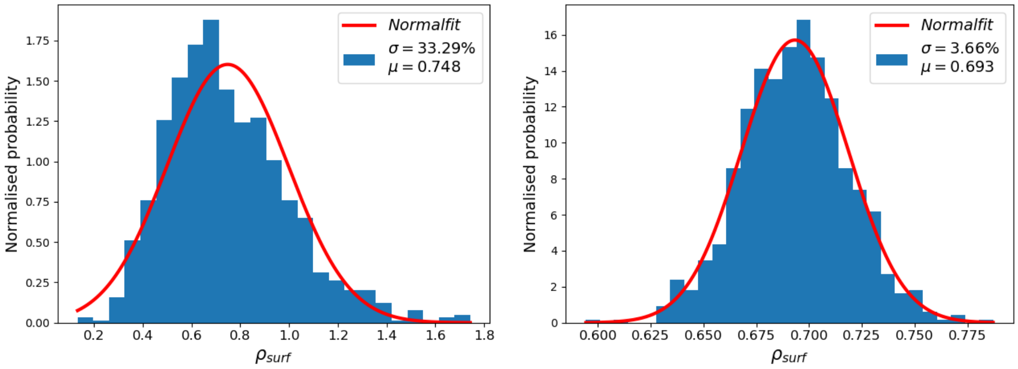

(c) B9 (d) B12

Figure 4: Surface reflectance for a set of bands in the Libya-4 desert obtained with the L2A-RUT code.

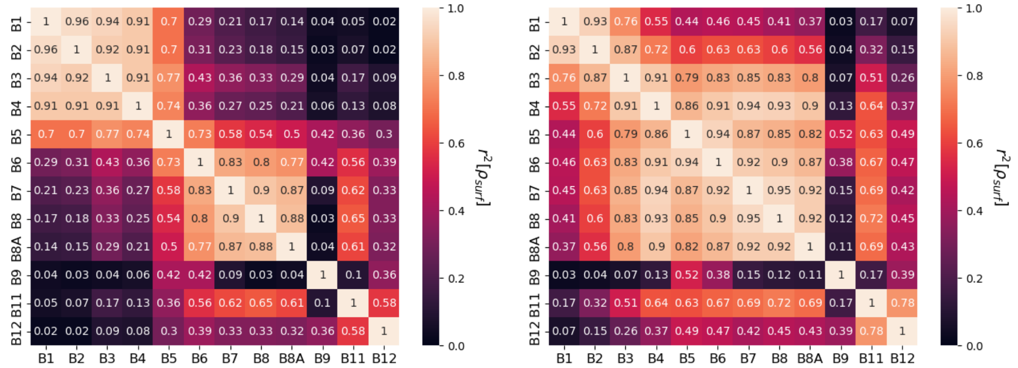

	B1	B2	B3	B4	B5	B6	B7	B8	B8A	B9	B11	B12
B1	1	0.96	0.94	0.91	0.7	0.29	0.21	0.17	0.14	0.04	0.05	0.02
B2	0.96	1	0.92	0.91	0.7	0.31	0.23	0.18	0.15	0.03	0.07	0.02
B3	0.94	0.92	1	0.91	0.77	0.43	0.36	0.33	0.29	0.04	0.17	0.09
B4	0.91	0.91	0.91	1	0.74	0.36	0.27	0.25	0.21	0.06	0.13	0.08
B5	0.7	0.7	0.77	0.74	1	0.73	0.58	0.54	0.5	0.42	0.36	0.3
B6	0.29	0.31	0.43	0.36	0.73	1	0.83	0.8	0.77	0.42	0.56	0.39
B7	0.21	0.23	0.36	0.27	0.58	0.83	1	0.9	0.87	0.09	0.62	0.33
B8	0.17	0.18	0.33	0.25	0.54	0.8	0.9	1	0.88	0.03	0.65	0.33
B8A	0.14	0.15	0.29	0.21	0.5	0.77	0.87	0.88	1	0.04	0.61	0.32
B9	0.04	0.03	0.04	0.06	0.42	0.42	0.09	0.03	0.04	1	0.1	0.36
B11	0.05	0.07	0.17	0.13	0.36	0.56	0.62	0.65	0.61	0.1	1	0.58
B12	0.02	0.02	0.09	0.08	0.3	0.39	0.33	0.33	0.32	0.36	0.58	1

(a) Amazon spectral error correlation

	B1	B2	B3	B4	B5	B6	B7	B8	B8A	B9	B11	B12
B1	1	0.93	0.76	0.55	0.44	0.46	0.45	0.41	0.37	0.03	0.17	0.07
B2	0.93	1	0.87	0.72	0.6	0.63	0.63	0.6	0.56	0.04	0.32	0.15
B3	0.76	0.87	1	0.91	0.79	0.83	0.85	0.83	0.8	0.07	0.51	0.26
B4	0.55	0.72	0.91	1	0.86	0.91	0.94	0.93	0.9	0.13	0.64	0.37
B5	0.44	0.6	0.79	0.86	1	0.94	0.87	0.85	0.82	0.52	0.63	0.49
B6	0.46	0.63	0.83	0.91	0.94	1	0.92	0.9	0.87	0.38	0.67	0.47
B7	0.45	0.63	0.85	0.94	0.87	0.92	1	0.95	0.92	0.15	0.69	0.42
B8	0.41	0.6	0.83	0.93	0.85	0.9	0.95	1	0.92	0.12	0.72	0.45
B8A	0.37	0.56	0.8	0.9	0.82	0.87	0.92	0.92	1	0.11	0.69	0.43
B9	0.03	0.04	0.07	0.13	0.52	0.38	0.15	0.12	0.11	1	0.17	0.39
B11	0.17	0.32	0.51	0.64	0.63	0.67	0.69	0.72	0.69	0.17	1	0.78
B12	0.07	0.15	0.26	0.37	0.49	0.47	0.42	0.45	0.43	0.39	0.78	1

(b) Libya4 spectral error correlation

Figure 5: S2 L2A spectral error correlation for Amazon site (Figure 5a) and desert site (Figure 5b)

At a first glance, it is clear that the spectral error correlation is very different for the two sites. The Amazon example shows a strong correlation between B1-B4 bands and B6-B8A bands. These bands correspond to those dominated by the atmosphere and the surface signal respectively. The error correlation for the desert case are significantly higher as a consequence of a much higher surface reflectance. The correlation tends to decrease with the spectral distance except in the case of B9. In that case, the band is uncorrelated with most of the bands except for those that have a minor sensitivity to water vapour.

3.2. GUM analytical vs. MCM multivariate approach

Subsection 2.4 described the methodology to obtain uncertainty estimates with a GUM analytical form. It was also mentioned the expected complexity of using this approach through a radiative transfer code due to non-linear nature and ad-hoc solutions.

This subsection implements the same examples as in subsection 3.1 and compares them to the GUM analytical solution. However, here we wanted to focus on the effect of the Libradtran radiative transfer and the uncertainty calculation only considers a uniform lambertian approach (i.e. equation 2 in subsection 2.2.5).

Figures 6 and 7 present the surface reflectance distribution for a set of L2A bands Figures C.30 and C.31 in Appendix C contain each one of the S2 L2A bands.

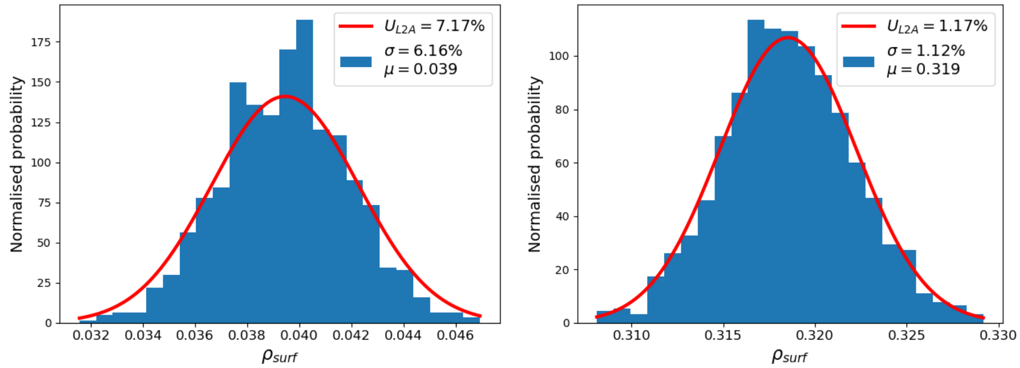

(a) B1

(b) B8

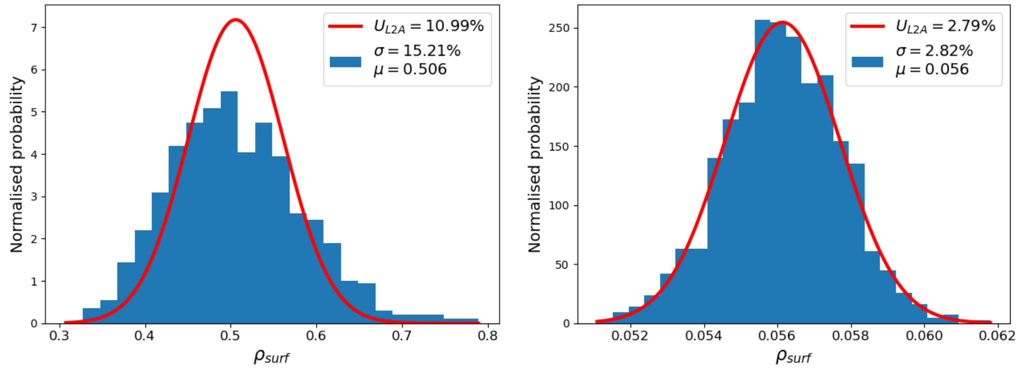

(c) B9

(d) B12

Figure 6: Surface reflectance for a set of bands in the Amazon case obtained for a uniform lambertian approach (i.e. equation 2 in subsection 2.2.5) for both the MCM multivariate and GUM analytical approach.

In general, most of the bands the agreement is acceptable. However, is for the bands that are most affected by AOT (B1) and water vapour (B9) where disagreements between a GUM analytical approach and MCM mulivariate appear. For B9, the disagreement is even more pronounced due to the large absorption of water vapour.

We have produced another example analogue to the one presented here but Libradtran has been parameterised with a water vapour level of 5 cm and AOT of 1.14 (approximately 5 km visibility). These values are extreme cases and represent the highest values stored in the pre-compiled LUT of Sen2Cor. Figures 8 and 9 present the surface reflectance distribution for a set of L2A bands Figures C.32 and C.33 in Appendix C contain each one of the S2 L2A

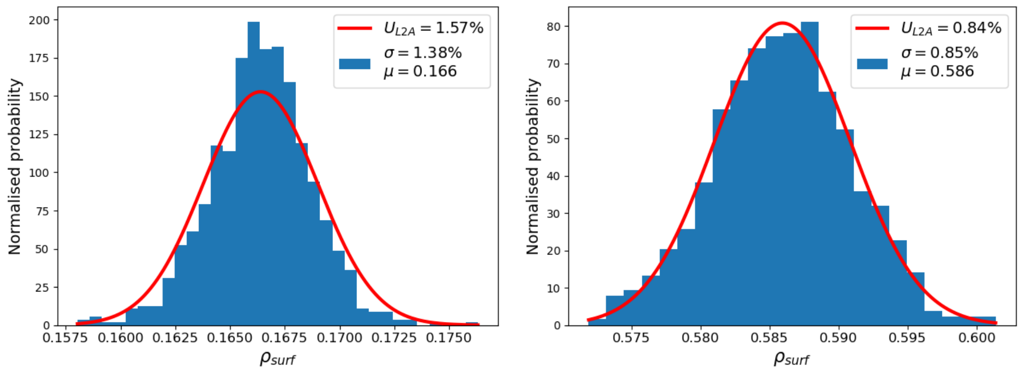

(a) B1

(b) B8

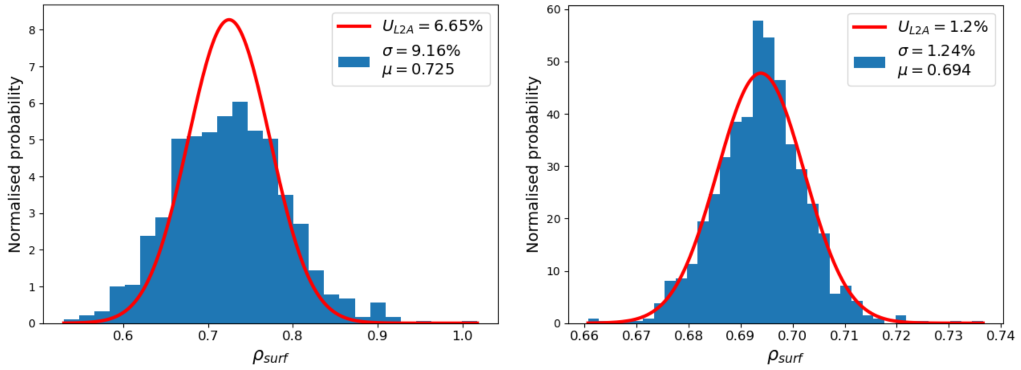

(c) B9

(d) B12

Figure 7: Surface reflectance for a set of bands in the Libya4 case obtained for a uniform lambertian approach (i.e. equation 2 in subsection 2.2.5) for both the MCM multivariate and GUM analytical approach.

bands.

The distribution for almost all the cases are highly non-normal and disagree with a GUM analytical framework. The agreement is only close for a highly reflectance surface such as Libya4 and bands with a negligible AOT and small water vapour sensitivity such as B11 and B12. Thus, these examples indicate that the GUM analytical approach is not valid when the atmosphere dominates over the surface signal.

On the other hand, some bands such as B1 and B2 in Figures 8 and 9 contain a large fraction of the distribution in negative values and some discontinuity on the right positive values. This is the result of a modelling of AOT uncertainty using a normal distribution and the impossibility of the

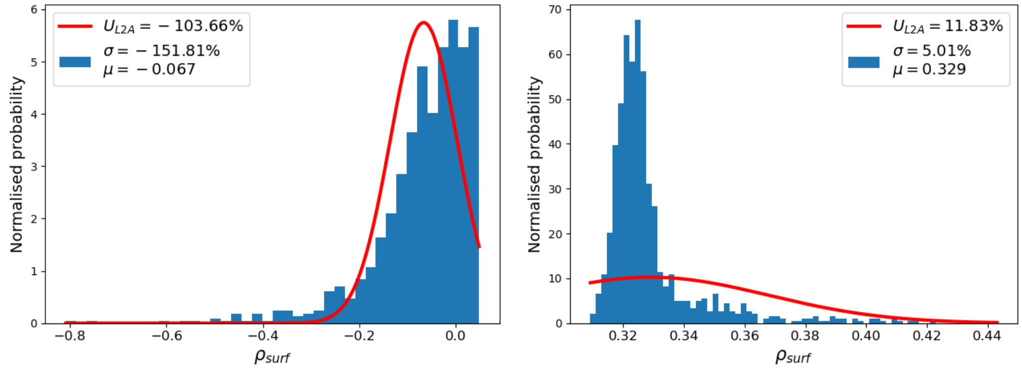

(a) B1

(b) B8

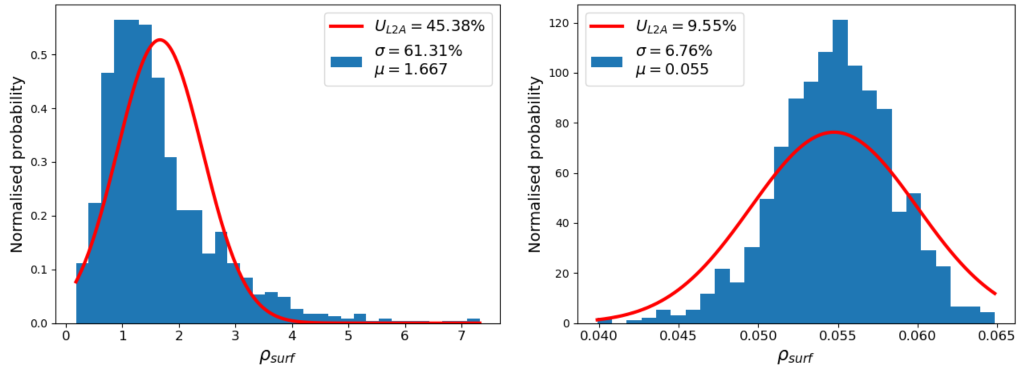

(c) B9

(d) B12

Figure 8: Surface reflectance for a set of bands in the Amazon case obtained for a uniform lambertian approach (i.e. equation 2 in subsection 2.2.5) for both the MCM mulitvariate and GUM analytical approach. The simulation was forced to set a value of 5 cm for water vapour and 1.14 (approximately 5 km visibility) for AOT.

radiative transfer to model negative AOT values. Thus, it suggests that a modelling of the AOT as a log-normal distribution might be a more adequate approach in these extreme events.

Figures 10 and 11 present the spectral error correlation between the L2A bands for the cases described before.

From these correlation matrices, one can observe how it is possible to obtain negative correlation between bands in the blue region (e.g. B1 and B2) and bands in the NIR region (e.g. B8). Figure 11 presents the most extreme results whereas Figure 10 only includes a small negative correlation between B1 and B8. Looking at equation 2, this negative correlation emerges

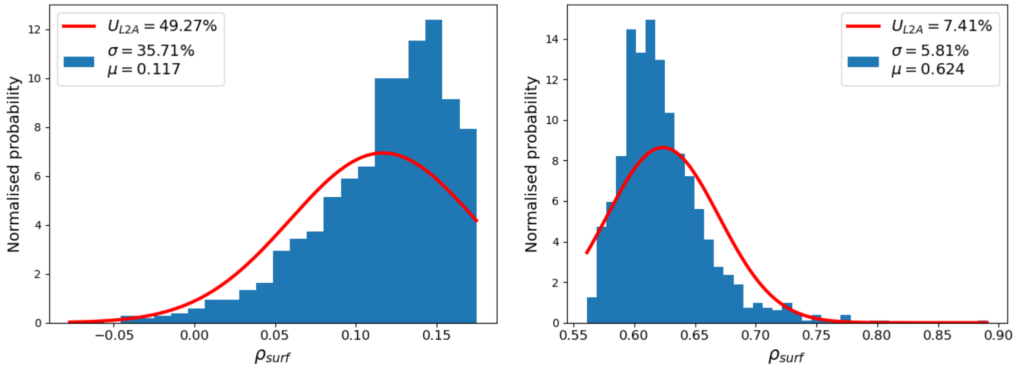

(a) B1

(b) B8

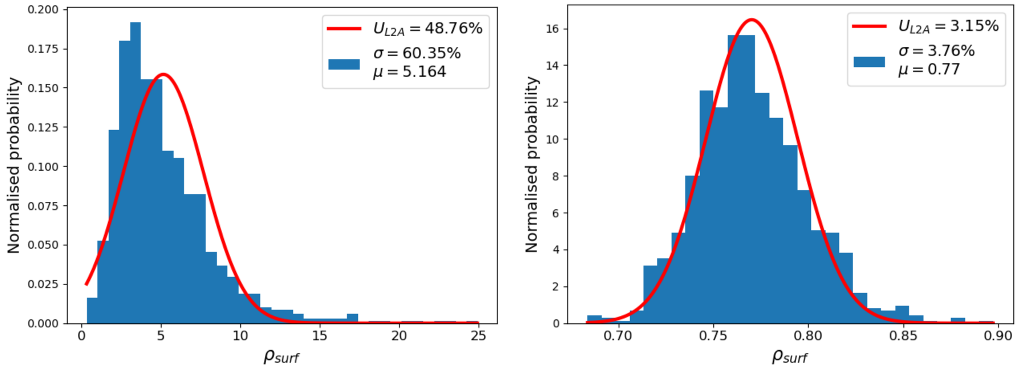

(c) B9

(d) B12

Figure 9: Surface reflectance for a set of bands in the Libya4 case obtained for a uniform lambertian approach (i.e. equation 2 in subsection 2.2.5) for both the MCM multivariate and GUM analytical approach. The simulation was forced to set a value of 5 cm for water vapour and 1.14 (approximately 5 km visibility) for AOT.

from the negative sensitivity of L_p. This term is highly dominant in bands dominated by the atmosphere signal (e.g. B1) and becomes negligible at higher wavelengths. Therefore, although this is a simplified case and other sources of uncertainty must be accounted, it is possible that under some scenarios of low surface reflectance and high AOT, the errors for some of the bands are negatively correlated.

Another interesting result is to observe that error in B12 is significantly correlated to B5 and B6. This is, for high water vapour levels the error in these bands, despite a large spectral distance, can be highly correlated.

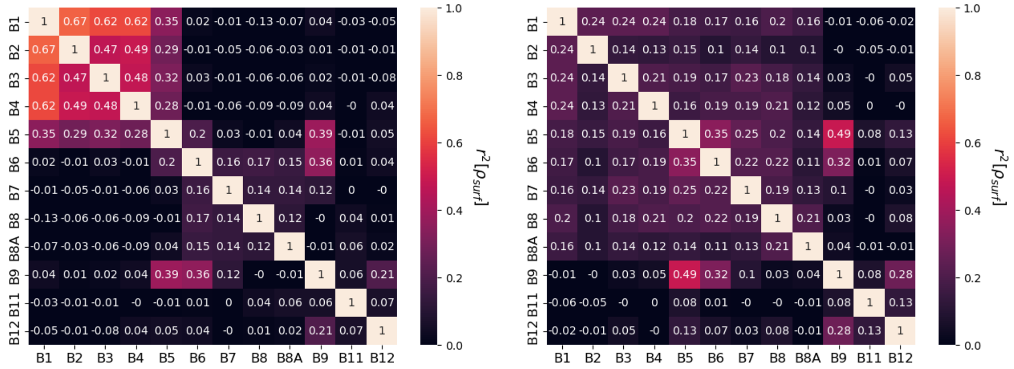

	B1	B2	B3	B4	B5	B6	B7	B8	B8A	B9	B11	B12
B1	1	0.67	0.62	0.62	0.35	0.02	-0.01	-0.13	-0.07	0.04	-0.03	-0.05
B2	0.67	1	0.47	0.49	0.29	-0.01	-0.05	-0.06	-0.03	0.01	-0.01	-0.01
B3	0.62	0.47	1	0.48	0.32	0.03	-0.01	-0.06	-0.06	0.02	-0.01	-0.08
B4	0.62	0.49	0.48	1	0.28	-0.01	-0.06	-0.09	-0.09	0.04	-0	0.04
B5	0.35	0.29	0.32	0.28	1	0.2	0.03	-0.01	0.04	0.39	-0.01	0.05
B6	0.02	-0.01	0.03	-0.01	0.2	1	0.16	0.17	0.15	0.36	0.01	0.04
B7	-0.01	-0.05	-0.01	-0.06	0.03	0.16	1	0.14	0.14	0.12	0	-0
B8	-0.13	-0.06	-0.06	-0.09	-0.01	0.17	0.14	1	0.12	-0	0.04	0.01
B8A	-0.07	-0.03	-0.06	-0.09	0.04	0.15	0.14	0.12	1	-0.01	0.06	0.02
B9	0.04	0.01	0.02	0.04	0.39	0.36	0.12	-0	-0.01	1	0.06	0.21
B11	-0.03	-0.01	-0.01	-0	-0.01	0.01	0	0.04	0.06	0.06	1	0.07
B12	-0.05	-0.01	-0.08	0.04	0.05	0.04	-0	0.01	0.02	0.21	0.07	1

(a) Amazon spectral error correlation

	B1	B2	B3	B4	B5	B6	B7	B8	B8A	B9	B11	B12
B1	1	0.24	0.24	0.24	0.18	0.17	0.16	0.2	0.16	-0.01	-0.06	-0.02
B2	0.24	1	0.14	0.13	0.15	0.1	0.14	0.1	0.1	-0	-0.05	-0.01
B3	0.24	0.14	1	0.21	0.19	0.17	0.23	0.18	0.14	0.03	-0	0.05
B4	0.24	0.13	0.21	1	0.16	0.19	0.19	0.21	0.12	0.05	0	-0
B5	0.18	0.15	0.19	0.16	1	0.35	0.25	0.2	0.14	0.49	0.08	0.13
B6	0.17	0.1	0.17	0.19	0.35	1	0.22	0.22	0.11	0.32	0.01	0.07
B7	0.16	0.14	0.23	0.19	0.25	0.22	1	0.19	0.13	0.1	-0	0.03
B8	0.2	0.1	0.18	0.21	0.2	0.22	0.19	1	0.21	0.03	-0	0.08
B8A	0.16	0.1	0.14	0.12	0.14	0.11	0.13	0.21	1	0.04	-0.01	-0.01
B9	-0.01	-0	0.03	0.05	0.49	0.32	0.1	0.03	0.04	1	0.08	0.28
B11	-0.06	-0.05	-0	0	0.08	0.01	-0	-0	-0.01	0.08	1	0.13
B12	-0.02	-0.01	0.05	-0	0.13	0.07	0.03	0.08	-0.01	0.28	0.13	1

(b) Libya4 spectral error correlation

Figure 10: S2 L2A spectral error correlation for Amazon site (Figure 10a) and Libya-4 site (Figure 10b) obtained for a uniform lambertian approach (i.e. equation 2 in subsection 2.2.5).

3.3. Case study: uncertainty propagation to vegetation indices

First results in subsection 3.1 illustrate the results at different scenes for the L2A products. In this subsection, we want to exemplify how they can be used in the propagation of a couple of largely-used vegetation indexes (normalised differential vegetation index (NDVI) and enhanced vegetation index (EVI)) and how critical the spectral error correlation is to define the output uncertainty.

Two parcels include in the S2 tile 32TMT from the S2 UTM projection have been selected. These parcels correspond to a winter barley parcel centered at lat,lon 8.696025314°,47.452876567°and a winter wheat parcel centered at lat,lon 8.697838380°,47.451120279°.

For this case study we have selected cloud-free acquisitions in the year 2022. Specifically, those are on the 22nd of March, the 21st of April, the 20th of June and the 25th of July. Figure 12 shows Sentinel-2 false-color infrared composites at 10 m spatial resolution. The selected dates reflect different phenological development stages of the two winter crops. Since barley has a faster phenological development cycle than wheat, some interesting observations can be made in Figure 12: On the first date (March 22nd) the canopy of the winter barley parcel is almost closed, i.e., the parcel appears reddish since no soil background is visible. In the case of winter wheat, the canopy coverage is lower as the plants are still in tillering stage. In April, the canopy coverage of the winter wheat parcel has increased. Two months

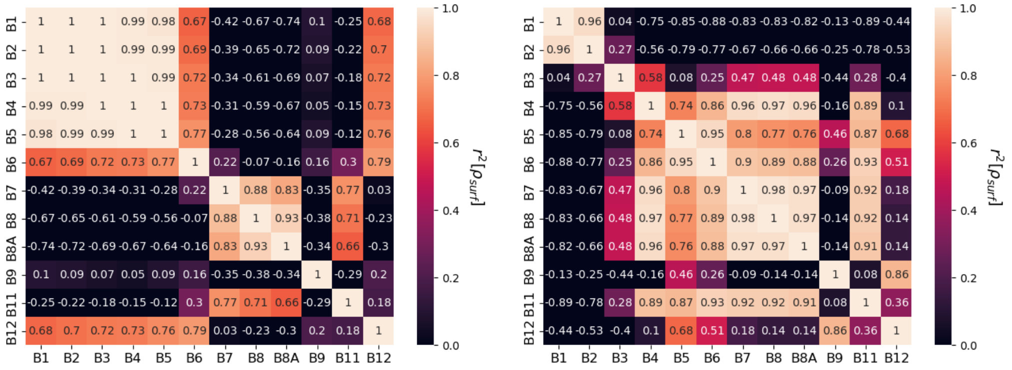

	B1	B2	B3	B4	B5	B6	B7	B8	B8A	B9	B11	B12
B1	1	1	1	0.99	0.98	0.67	-0.42	-0.67	-0.74	0.1	-0.25	0.68
B2	1	1	1	0.99	0.99	0.69	-0.39	-0.65	-0.72	0.09	-0.22	0.7
B3	1	1	1	1	0.99	0.72	-0.34	-0.61	-0.69	0.07	-0.18	0.72
B4	0.99	0.99	1	1	1	0.73	-0.31	-0.59	-0.67	0.05	-0.15	0.73
B5	0.98	0.99	0.99	1	1	0.77	-0.28	-0.56	-0.64	0.09	-0.12	0.76
B6	0.67	0.69	0.72	0.73	0.77	1	0.22	-0.07	-0.16	0.16	0.3	0.79
B7	-0.42	-0.39	-0.34	-0.31	-0.28	0.22	1	0.88	0.83	-0.35	0.77	0.03
B8	-0.67	-0.65	-0.61	-0.59	-0.56	-0.07	0.88	1	0.93	-0.38	0.71	-0.23
B8A	-0.74	-0.72	-0.69	-0.67	-0.64	-0.16	0.83	0.93	1	-0.34	0.66	-0.3
B9	0.1	0.09	0.07	0.05	0.09	0.16	-0.35	-0.38	-0.34	1	-0.29	0.2
B11	-0.25	-0.22	-0.18	-0.15	-0.12	0.3	0.77	0.71	0.66	-0.29	1	0.18
B12	0.68	0.7	0.72	0.73	0.76	0.79	0.03	-0.23	-0.3	0.2	0.18	1

(a) Amazon spectral error correlation

	B1	B2	B3	B4	B5	B6	B7	B8	B8A	B9	B11	B12
B1	1	0.96	0.04	-0.75	-0.85	-0.88	-0.83	-0.83	-0.82	-0.13	-0.89	-0.44
B2	0.96	1	0.27	-0.56	-0.79	-0.77	-0.67	-0.66	-0.66	-0.25	-0.78	-0.53
B3	0.04	0.27	1	0.58	0.08	0.25	0.47	0.48	0.48	-0.44	0.28	-0.4
B4	-0.75	-0.56	0.58	1	0.74	0.86	0.96	0.97	0.96	-0.16	0.89	0.1
B5	-0.85	-0.79	0.08	0.74	1	0.95	0.8	0.77	0.76	0.46	0.87	0.68
B6	-0.88	-0.77	0.25	0.86	0.95	1	0.9	0.89	0.88	0.26	0.93	0.51
B7	-0.83	-0.67	0.47	0.96	0.8	0.9	1	0.98	0.97	-0.09	0.92	0.18
B8	-0.83	-0.66	0.48	0.97	0.77	0.89	0.98	1	0.97	-0.14	0.92	0.14
B8A	-0.82	-0.66	0.48	0.96	0.76	0.88	0.97	0.97	1	-0.14	0.91	0.14
B9	-0.13	-0.25	-0.44	-0.16	0.46	0.26	-0.09	-0.14	-0.14	1	0.08	0.86
B11	-0.89	-0.78	0.28	0.89	0.87	0.93	0.92	0.92	0.91	0.08	1	0.36
B12	-0.44	-0.53	-0.4	0.1	0.68	0.51	0.18	0.14	0.14	0.86	0.36	1

(b) Libya4 spectral error correlation

Figure 11: S2 L2A spectral error correlation for Amazon site (Figure 11a) and Libya-4 site (Figure 11b) obtained for a uniform lambertian approach (i.e. equation 2 in subsection 2.2.5). The simulation was forced to set a value of 5 cm for water vapour and 1.14 (approximately 5 km visibility) for AOT.

later (June 20th) the winter barley has been harvested and the winter wheat canopy enters the senescence phase. At the end of July, also the winter wheat parcel has been harvested, and a cover crop is grown on the former winter barley parcel.

We have processed each one of the data products to obtain a per-band 1000 surface reflectance samples. These samples, here referred as *measured*, inherently incorporate the spectral error correlation between the S2 bands. They are propagated to obtain a same number of samples for both NDVI(Rouse et al.) and EVI(Huete et al.) at each day and location as follows:

$$NDVI = \frac{B08 - B04}{B08 + B04} \tag{9}$$

$$EVI = 2.5\frac{B08 - B04}{B08 + 6B04 - 7.5B02 + 1} \tag{10}$$

Two more calculations have been generated to illustrate the same scenarios but where the samples include full spectral error correlation (here we refer to them as *correlated*) and no spectral error correlation (referred as *uncorrelated*).

The results for these three cases at each site are shown in Figure 13.

The values of both NDVI and EVI values are, as expected, highly correlated in the upper panels in Figure 13 with ranging values from 0.8, close to the maximum of the vegetation growth, to 0.2 right after harvesting. The middle

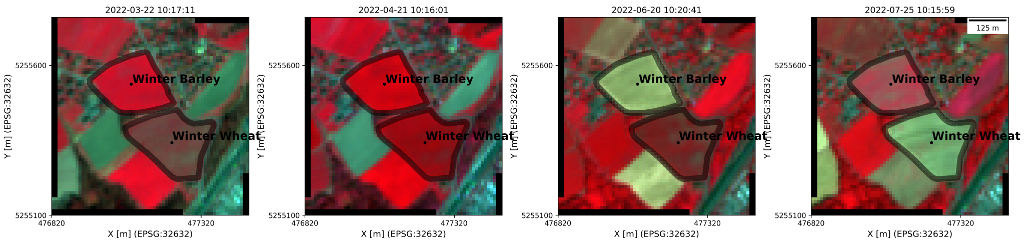

Figure 12: Selected parcels for the case study on the 22nd of March, the 21st of April, the 20th of June and the 25th of July . Upper left parcel contains winter barley (centered at lat,lon: 47.452876567°,8.696025314°) and bottom right parcel contains winter wheat (centered at lat,lon: 47.451120279°,8.697838380°)

panels represent the NDVI relative uncertainty for the three spectral error correlation scenarios previously commented. The *measured* uncertainty moves in between 2 and 4% but it always fluctuates between the *correlated* and *uncorrelated* cases. Similarly to the work in Graf et al. (2023), these two cases represent the opposite cases and for an NDVI they also represent the potential uncertainty boundaries. A similar situation occurs for the EVI uncertainty (bottom panels in Figure 13) but in this case, the *measured* uncertainty is closer to the *correlated* case with marginally lower values. Note that this coefficient is generated using three bands (see Eq. 10) with negative coefficient for B2. The error combination between these bands largely depends on the cancellation of these bands.

In general, we appreciate how important the spectral error correlation is in order to propagate the L2A product uncertainty. Table 1 contains the correlation between B2, B4 and B8 L2A bands for the studied parcels and dates.

Here, the correlation trend of B8 vs. B4 follows an inverse relationship to the NDVI trend. In the case of EVI, the correlation trends of B2 vs. B4 and B2 vs. B8 are inversely related. Thus, the spectral error correlation matrix indicates a strong dependence on the phenological cycle that not only determines the propagated uncertainties but also the observation space for any advanced retrieval (e.g. see Maahn et al. (2020)).

Table 1: Spectral error correlation between B2, B4 and B8 L2A bands for winter barley and winter wheat fields on the 22nd of March, the 21st of April, the 20th of June and the 25th of July.

Acquisition date	22nd March	21st April	20th June	25th July
Winter barley				
B4-B8 correlation	0.14	0.06	0.82	0.66
B2-B4 correlation	0.9	0.94	0.7	0.8
B2-B8 correlation	0.05	0.05	0.38	0.33
Winter wheat				
B4-B8 correlation	0.44	0.16	0.5	0.82
B2-B4 correlation	0.85	0.94	0.9	0.68
B2-B8 correlation	0.21	0.08	0.29	0.38

4. Discussion

4.1. Main findings

The subsection 3.1 presents two examples (one for the Amazon forest and the other for Sahara dune desert) that were useful to test the code and examine the first results.

The first interesting point is that, in comparison to the L1C uncertainty estimates, the L2A uncertainty estimates are larger in relative terms and present a larger spectral band dependence. That is, the range of relative uncertainty at L1C moves from 1 to 3% for the examples to 3-20% for the L2A uncertainty estimates with larger values. This is an expected situation since some bands are almost not affected by the atmospheric correction while others are largely dominated by the atmosphere. For those bands with little impact of the atmosphere, the surface reflectance distribution is largely normal. However, this is not the case for B9 which is very sensitive to water vapour. This is also the case for the bands B1-B4 in the Amazon forest example but at a minor extent.

There are important differences between the two sites not only at uncertainty levels but more importantly on their spectral error correlation. The Amazon example shows a strong correlation between B1-B4 bands and B6-B8A bands separately as a consequence of the vegetation red-edge. The error correlation in the desert case is higher due to the higher surface reflectance with a dependence on the spectral distance.

We explored in detail the non-normal distribution of the surface reflectance found in the examples of subsection 3.1. Comparing to a GUM analytical approach (see subsection 2.4), the study in subsection 3.2 has illustrated the limits of assuming normal distributions and linear responses. It indicates that the GUM analytical approach is not valid in all L2A scenarios and, thus, its application at a global scale is limited. The comparison shows that for B1 (mostly affected by AOT) and B9 (mostly affected by water vapour) the results between the two methods generally disagree. However, when we set extreme atmospheric conditions with water vapour level of 5 cm and AOT of 1.14 (approximately 5 km visibility) the results between the two methods completely disagree for all bands.

In general, the GUM analytical method is valid as long as the atmosphere is not dominant. Any band that is highly sensitive to atmospheric absorption and scattering will be affected. For S2 satellite mission this occurs for some bands and scenes. That is, the proposed methodology proposed in subsection 2.4 has a limited application at a global scale. Upcoming Copernicus satellite missions such as CHIME or S2-NG will include a larger and narrower number of bands. It is expected then, that the use of multivariate MCM rather than a GUM analytical approach is even more recommended.

Subsection 3.1 has also shown that it is not unreasonable that the error of some L2A bands is negatively correlated. The spectral error correlation matrices in Figures 10 and 11 show that negative correlation between B1-B5 against B7-B8A is possible. The path radiance L_p substract the TOA radiance L_{TOA} in equation 2. The correlation between a band that is dominated by the atmospheric signal and one that is not might result in this negative error correlation.

Finally, the case study in subsection 3.3 shows the importance of bringing not only surface reflectance estimates but also spectral error correlation matrices to be able to propagate the uncertainty to biogeophysical variables and the phenological cycle. Importantly, the spectral error correlation matrix is largely dependent on the phenological cycle and the use of this information to define the observation space (i.e. here the L2A surface reflectance distribution) might introduce important improvements in biogeophysical retrievals (Maahn et al., 2020).

4.2. Further work in next versions

Although a large number of uncertainty sources are included, some of them are not yet available at this version. Under some scenarios, it is possible that these results in a small underestimation of the current L2A uncertainty levels. However, it is the idea that subsequent versions of this software include refined and/or novel uncertainty sources.

The work in Gorroño et al. (2017) describes the missing contributions for the L1C uncertainty estimates. These are effects such as spectral response, polarisation or orthorectification that depend on the scene. Relevant improvements are on-going to model these contributions. For example, the work in Toulemont et al. (2021) describes the efforts to provide in the upcoming S2 satellite units (C/D) a per-pixel spectral response. This type of information is critical to model the error (or potential correction) accross the focal plane. The orthorectification of the S2 data products at L1C (TOA reflectance) has been also studied in Gorroño and Guanter (2021). This process slightly impacts both the uncertainty and correlation structure. The study explores potential methodologies to evaluate both the noise change and the interpolation accuracy. However, further development of this work is still needed to include these L1C contributions in future versions of the uncertainty estimates.

The work here presented includes the uncertainty associated to the atmospheric correction that is applied to the S2 L2A data products. The contributions described in subsection 2.2 include the most relevant effects of this process. However, there are specific corrections that are not considered here. Both the terrain and cirrus correction are included as an option in the Sen2Cor software and should be specifically studied in subsequent revisions. Sen2Cor also contains a LUT with pre-compiled values for the atmospheric functions at different parameterisations. Thus, in a real-scenario the atmospheric functions are interpolated values from the LUT. The assessment of these contributions would require, similarly to the orthorectification process, not only to understand the interpolation error but at which level impacts the error correlation structure.

The examples in Figures 8 and 9 and discussed in subsection 3.2 presented discontinuities in the distribution due to AOT levels restricted to positive values. This indicates that some of the input uncertainty such as AOT or water vapour might be better modelled with a log-normal or similar distribution. Furthermore, the proposed uncertainty estimates for these two input contributions are based on current validation efforts from the S2 quality team (S2 MSI ESL team, 2023) (see subsection 2.2.2). This is a continuous effort and future updates might consider more detailed information such as a per-biome uncertainty.

As commented in subsection 2.3, the code includes a special running mode that, rather than considering REPTRAN band model, considers the REPTRAN band model with medium spectral resolution (5 cm^{-1}) at 0.1 nm sampling. The REPTRAN model parameterises spectral bands of different widths as well as a number of instrument channels (Gasteiger et al., 2014). This parameterisation considerably reduces the processing and is sufficiently accurate for most scenarios. However, in some cases it might introduce differences in absolute values (mainly atmospheric absorption areas). First tests with this mode, show that the correlation among different atmospheric parameters largely changes. However, the spectral error correlation of the resulting surface reflectance uncertainty included only slightly differences in correlation for B1 and B2 with the rest of the bands. This mode also accounts for the TOA irradiance uncertainty. Interestingly, first results indicate that the error of TOA irradiance is cancelled out as expected but for larger values of L^{path}, the cancellation is not complete and both uncertainty and spectral error correlation are slightly affected. Further tests and verification should clarify the level of impact under different scenarios.

Finally, one of the most important novelties in this study is the consideration of spectral error correlation through the entire processing chain. Uncertainty contributions here are assigned spectral error correlation matrices dependent on the spectral distance and the focal plane (VNIR or SWIR). Nonetheless, we are aware that the information available is limited and contributions like *Libradtran uncertainty* and *lambertian assumption* (see subsections 2.2.5 and 2.2.4 respectively) have a strong impact on the final budget. In general, the attachment of spectral error correlation information in pre-flight calibration certificates or atmospheric studies should be encouraged in future studies.

4.3. Towards an operational version

The proposed multivariate MCM is computationally expensive and the amount of information at a pixel-level becomes prohibitive.

Concerning the processing requirements, a potential solution is that satellite operators (e.g. space agencies) implement a similar approach to the one here presented in a cloud environment with large processing capabilities. This would allow users to a rapid access to queries for an uncertainty and spectral error correlation assessment of a pixel or set of them. Furthermore, the possibility to be built as an extension of the ground processing would benefit from the *know-how* of the satellite mission team as well as a constant update of the satellite mission performance and processing baseline.

The calculation of the uncertainty and spectral error correlation for a single pixel, area or set of pixels does not constitute a major challenge in terms of data volumes. However, the per-pixel calculation and storage of these data volumes might become unfeasible. Upcoming Copernicus satellite missions such as CHIME or S2-NG (**?**)Celesti2022) will further increase the demand with a larger set of bands and higher spatial resolution. Thus, alternatives must be sought for a global distribution of this information.

In the last years, it is common practice to consider emulators as fast approximations of the atmospheric correction model. We can find already examples such as the one in Vicent et al. (2021) where they achieved an emulator with an accuracy <1% (k=2) with respect to MODTRAN radiative transfer. Another example in Brodrick et al. (2021) proposes a surrogate model to generate a candidate result that is refined with an emulator that corrects for the difference between the surrogate model and a complex accurate radiative transfer model. Thus, these types of models could be instrumental to deliver not only uncertainty but also spectral error correlation or error distributions at a pixel-level to the users.

4.4. Bayesian atmospheric correction

The current S2 L2A data products are generated with the Sen2Cor processor Louis et al. (2016). An alternative atmospheric correction method is to consider the mapping between TOA observations and surface reflectance with an optimal estimation method (Rodgers, 2000) or other Bayesian methods. For example, the work in Yin et al. (2022) implemented an alternative atmospheric correction for S2. Compared to a multivariate MCM and a GUM analtyical approach (see subsections 2.3 and 2.4), this method has the advantage to directly offer the variance matrix (both uncertainty and spectral error correlation matrix) in the retrieved space. However, the uncertainty propagation in optimal estimation relies on prior data that does not necessarily approximate the real scene such as in the case of extreme events. Furthermore, it also assumes normal distribution, unbiased measurements and moderately linear Jacobian matrix (Maahn et al., 2020).

The approach here presented can be used to cross-compare or flag the conditions in which optimal estimation assumptions might fail. A similar cross-comparison as in subsection 3.2 can be applied to, for example, identify scenarios where the Jacobian of the atmospheric model might not be sufficiently linear. Indeed, it is possible not only to identify but also to adapt these Bayesian frameworks so that these limitations are (partially) overcome. For example, the work in Braverman et al. (2021) also defines a multivariate MCM sampling of the Bayesian retrieval algorithm so that the retrieved covariance matrix accounts for the model discrepancy.

5. Conclusions

We presented the L2A-RUT software tool (available at Gorroño (2023)) that delivers both uncertainty estimates and spectral error correlation from the S2 L2A data products (i.e. surface reflectance). The methodology considers the uncertainty of the S2 L1C data products and the atmospheric correction. We have set a Multivariate MonteCarlo model that accounts for the spectral error correlation between S2 L2A bands and propagates the uncertainty of the L1 TOA reflectance, atmospheric parameterisation and adjacency correction. On the top of this propagation we also model the contributions from the Lambertain assumption and the estimated accuracy of the atmospheric radiative transfer. The results over a forest and desert scene illustrate the large variations both in uncertainty levels and spectral error correlation that can be found between data products. The example over vegetation metrics indicates a strong dependence of the error covariance matrix with the phenological cycle and highlights how relevant the spectral information is for the uncertainty propagation in end-user applications. Moreover, the spectral error correlation determines a better constrain of the observation space that can be beneficial in many advanced retrievals. The current tool version here presented delivers information to the user for a selected pixel or mean area. Based on this framework and first implementation, it is possible to explore efficient techniques such as machine learning models that in the near-future deliver operational global per-pixel uncertainty and spectral error correlation to the users.

Code availability

The code is released under the GNU General Public License v3.0. The repository can be accessed at `https://github.com/gorronyo/S2-L2A-RUT` and the release v1.0.0 can be download from there or Zenodo Gorroño (2023).

Declaration of Competing Interest

The authors declare that they have no known competing financial interests or personal relationships that could have appeared to influence the work reported in this paper.

Acknowledgements

Javier Gorroño is funded by the ESA Living Planet fellowship (ESA contract no. 4000130980/20/I-NS).

Appendix A. Amazon results

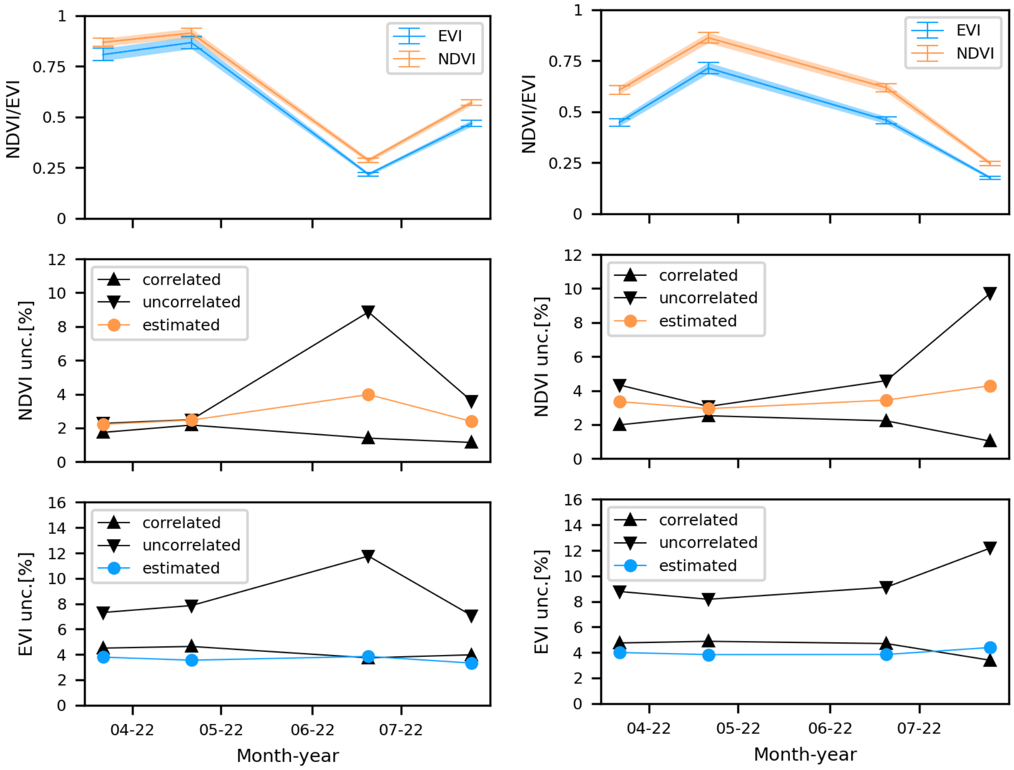

(a) Winter barley field

(b) Winter Wheat field

Figure 13: NDVI and EVI results at a winter barley field (Figure 13a) and a winter wheat field (Figure 13b) described in Figure 12 on the 22nd of March, the 21st of April, the 20th of June and the 25th of July. The upper panel illustrates the NDVI and EVI value trends. Middle and bottom panels represent the uncertainty in percent units of NDVI and EVI respectively. Here the labels *correlated*, *uncorrelated* and *measured* labels represent the case with no full spectral error correlation, no spectral error correlation and estimated spectral error correlation

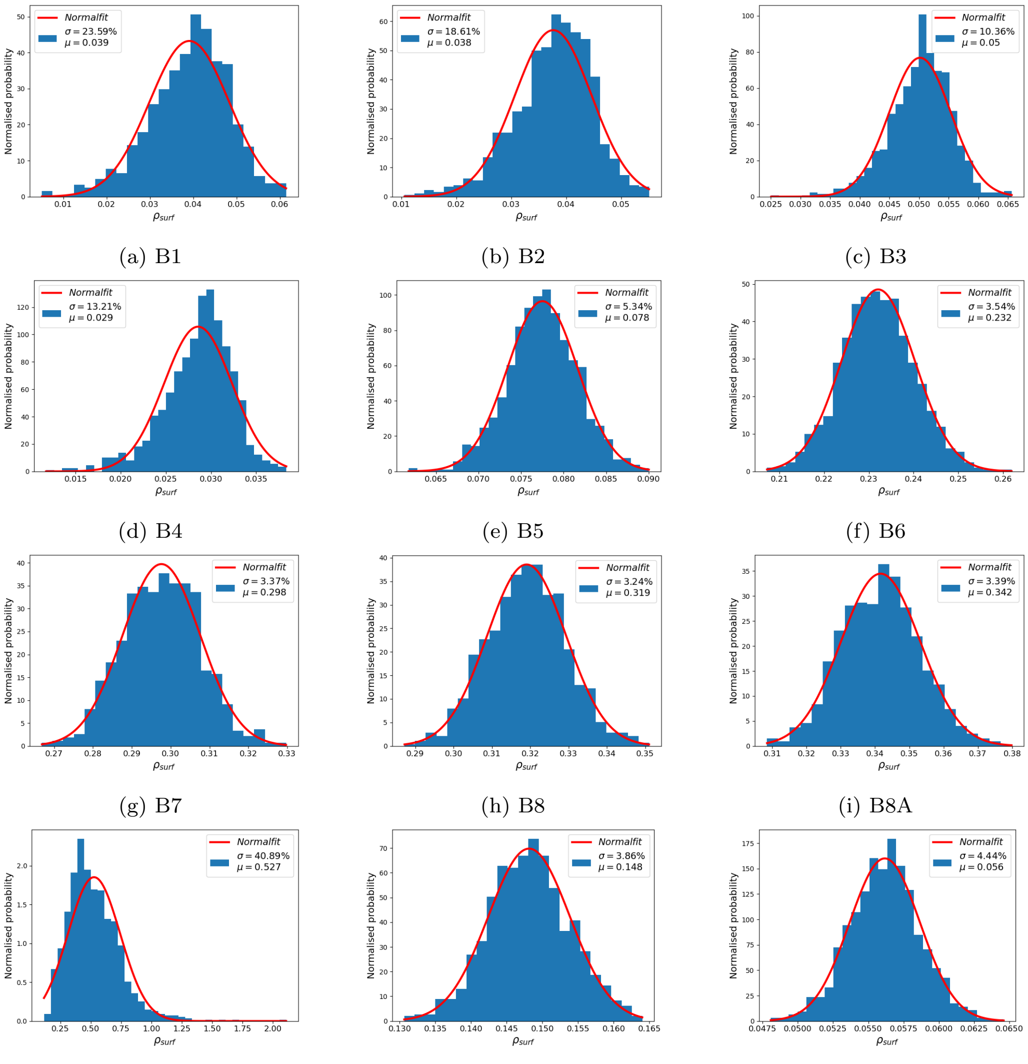

(a) B1 (b) B2 (c) B3

(d) B4 (e) B5 (f) B6

(g) B7 (h) B8 (i) B8A

(j) B9 (k) B11 (l) B12

Figure A.14: Surface reflectance Amazon

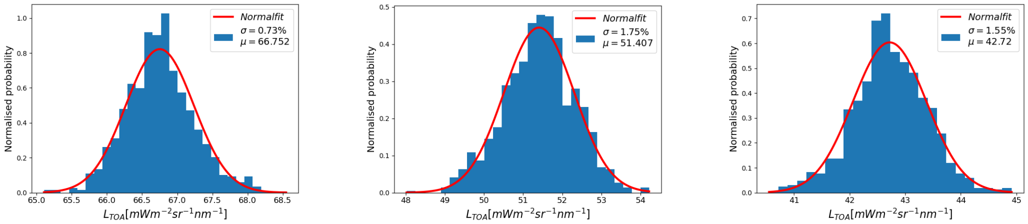

(a) B1 (b) B2 (c) B3

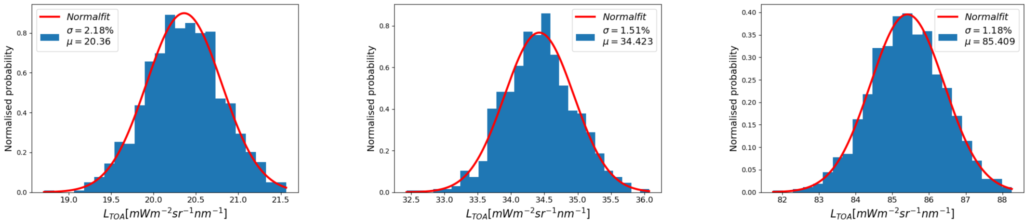

(d) B4 (e) B5 (f) B6

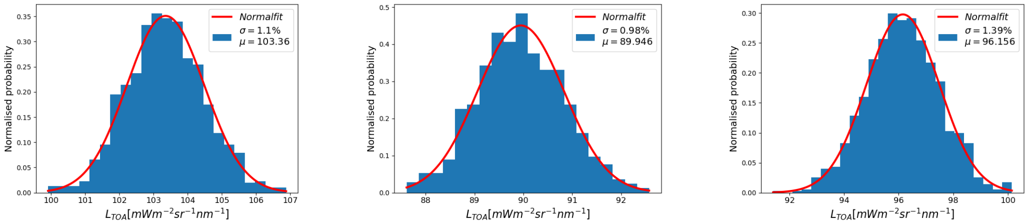

(g) B7 (h) B8 (i) B8A

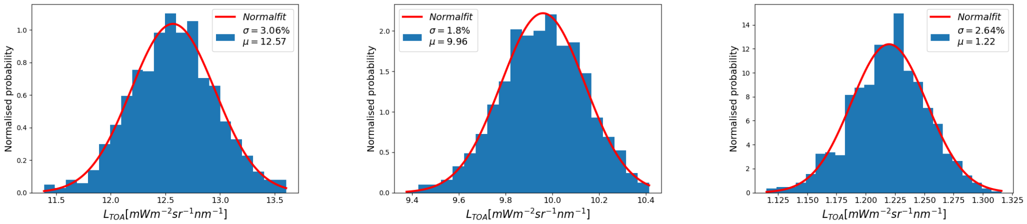

(j) B9 (k) B11 (l) B12

Figure A.15: TOA radiance Amazon

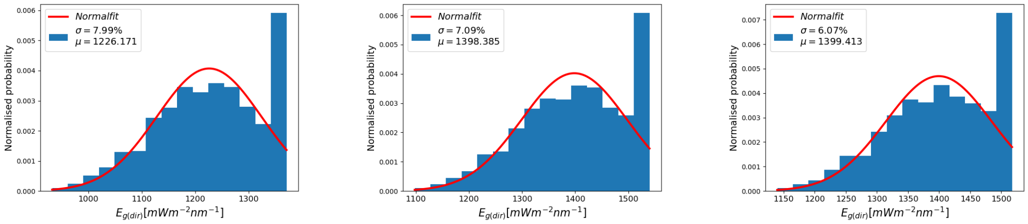

(a) B1 (b) B2 (c) B3

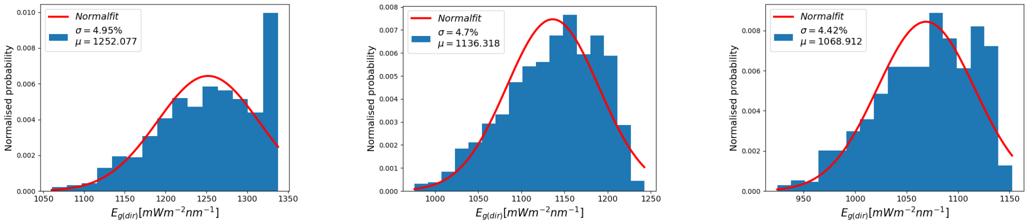

(d) B4 (e) B5 (f) B6

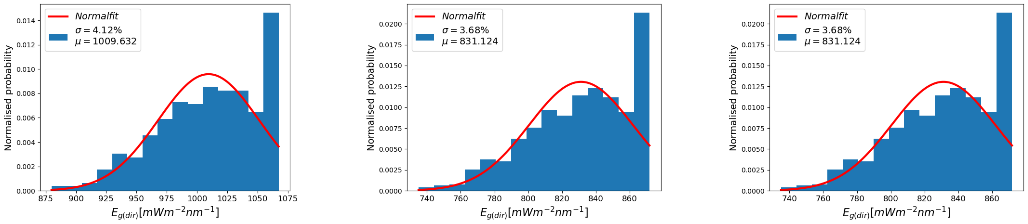

(g) B7 (h) B8 (i) B8A

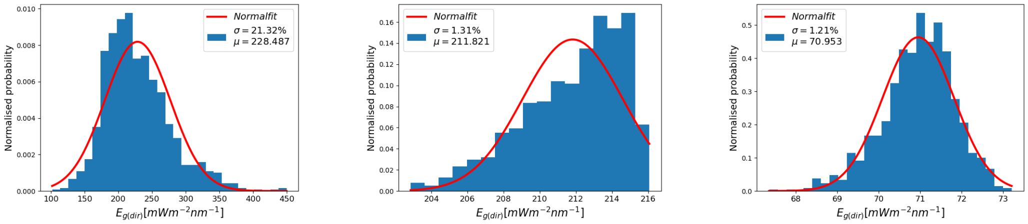

(j) B9 (k) B11 (l) B12

Figure A.16: Downwelling direct irradiance Amazon

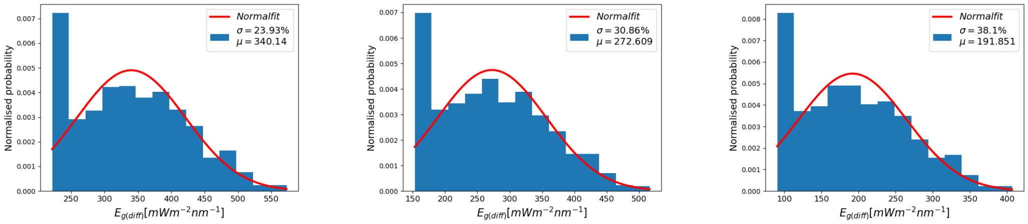

(a) B1 (b) B2 (c) B3

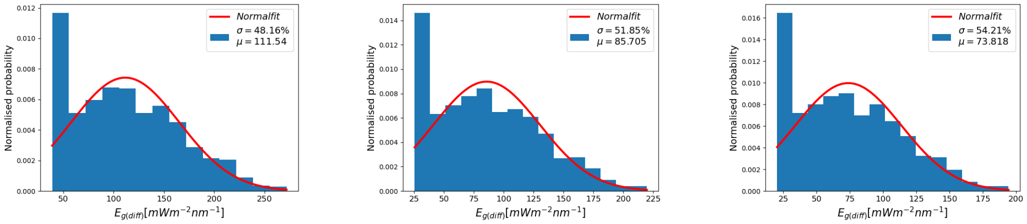

(d) B4 (e) B5 (f) B6

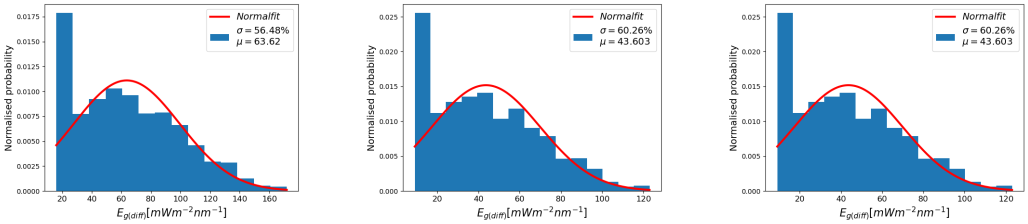

(g) B7 (h) B8 (i) B8A

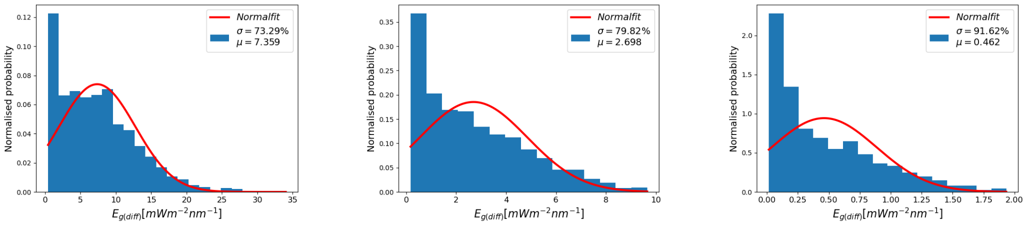

(j) B9 (k) B11 (l) B12

Figure A.17: Downwelling diffuse irradiance Amazon

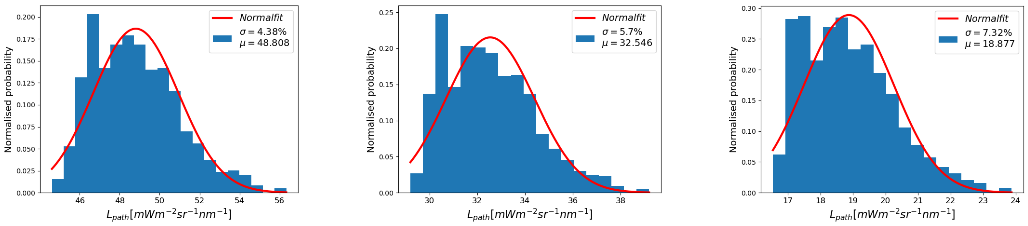

(a) B1 (b) B2 (c) B3

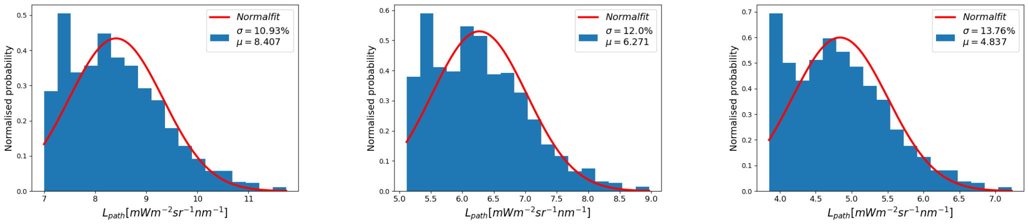

(d) B4 (e) B5 (f) B6

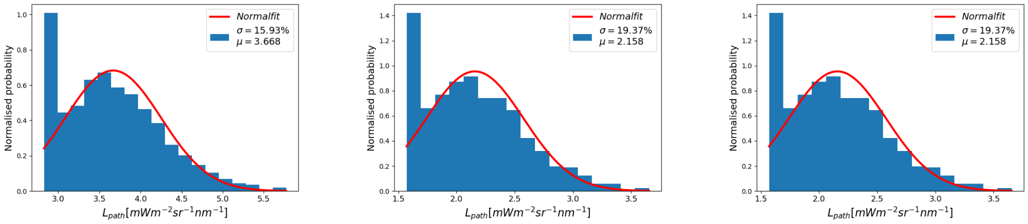

(g) B7 (h) B8 (i) B8A

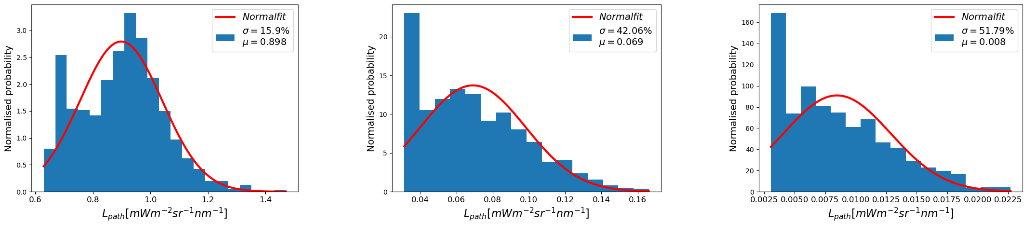

(j) B9 (k) B11 (l) B12

Figure A.18: Path radiance Amazon

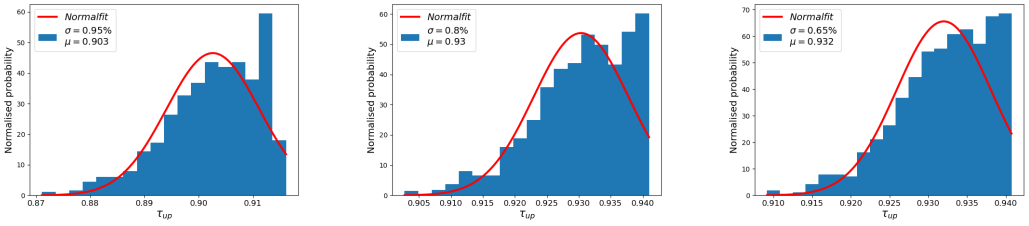

(a) B1 (b) B2 (c) B3

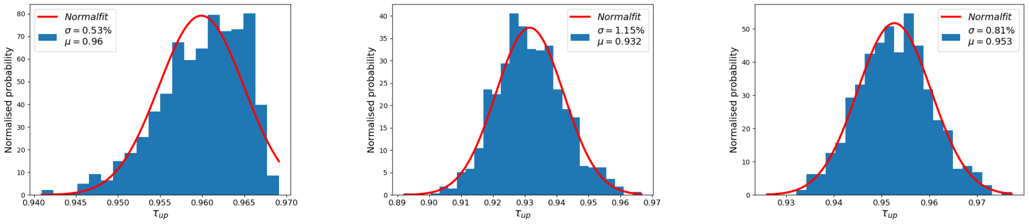

(d) B4 (e) B5 (f) B6

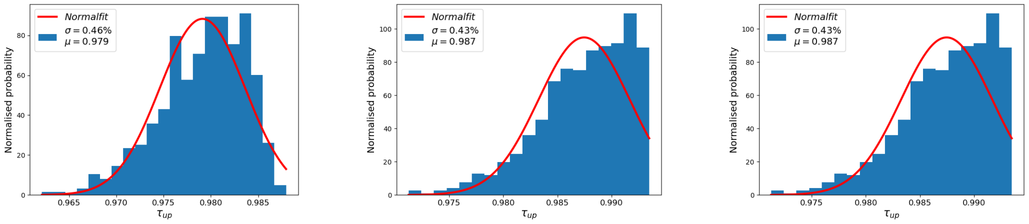

(g) B7 (h) B8 (i) B8A

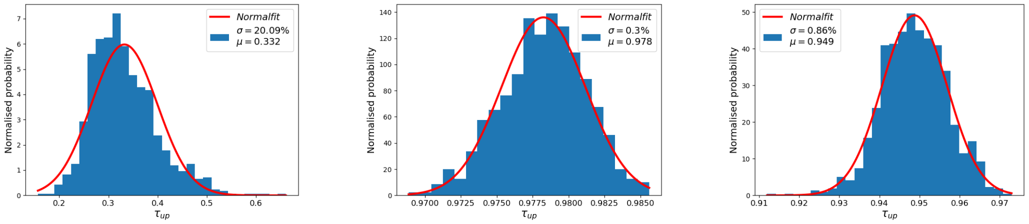

(j) B9 (k) B11 (l) B12

Figure A.19: Ground-to-TOA transmittance Amazon

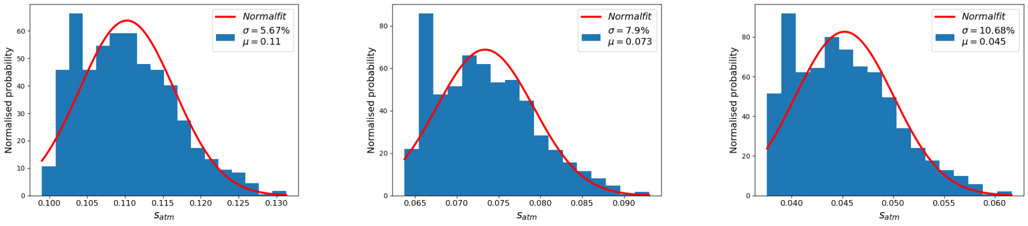

(a) B1 (b) B2 (c) B3

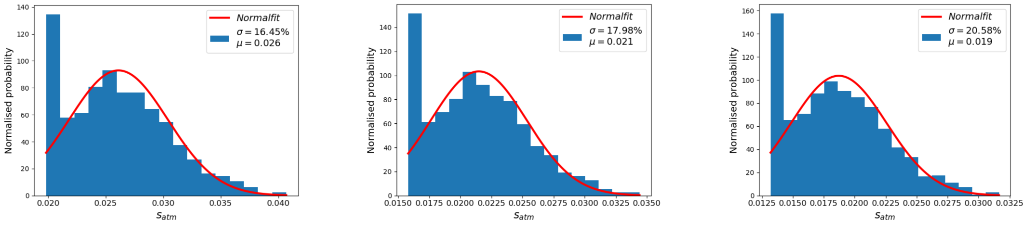

(d) B4 (e) B5 (f) B6

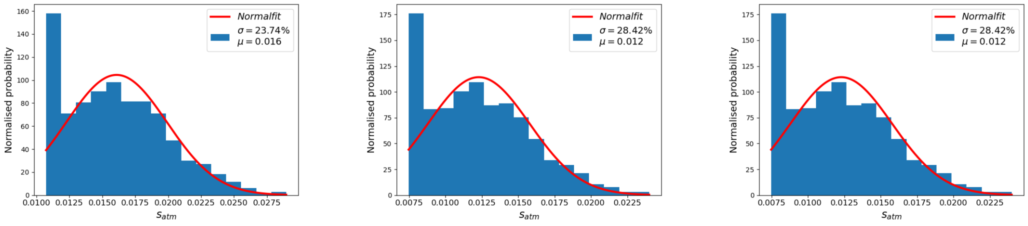

(g) B7 (h) B8 (i) B8A

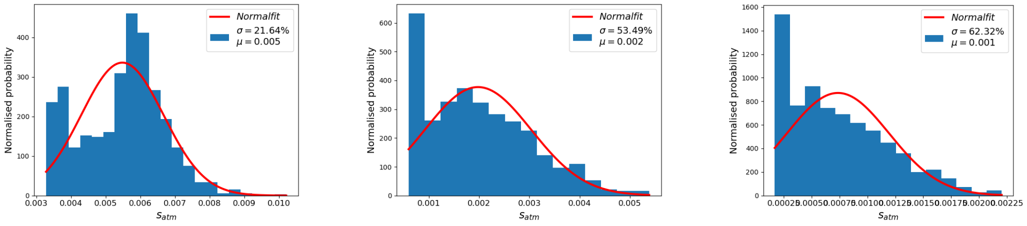

(j) B9 (k) B11 (l) B12

Figure A.20: Spherical albedo Amazon

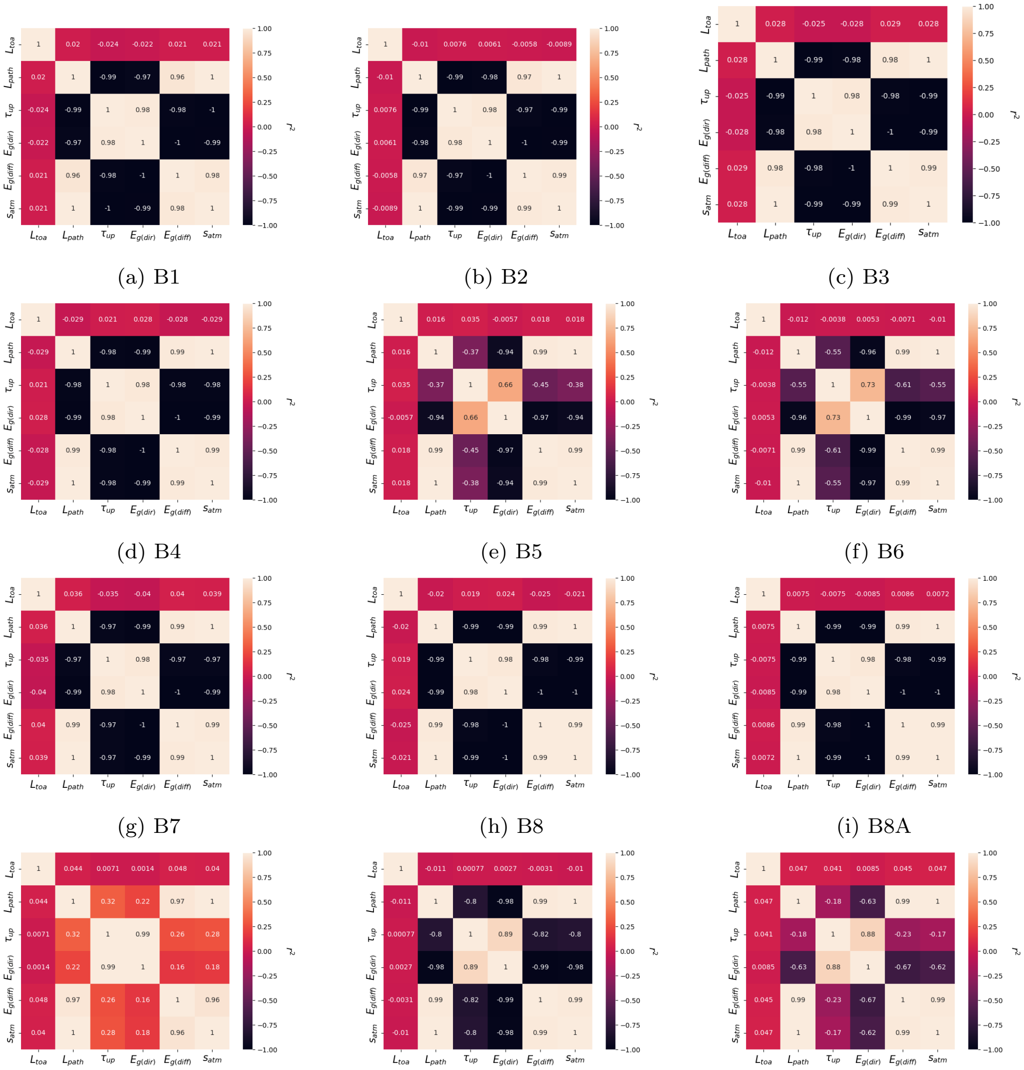

(a) B1 (b) B2 (c) B3

(d) B4 (e) B5 (f) B6

(g) B7 (h) B8 (i) B8A

(j) B9 (k) B11 (l) B12

Figure A.21: Atmospheric function correlation Amazon

Appendix B. Libya-4 results

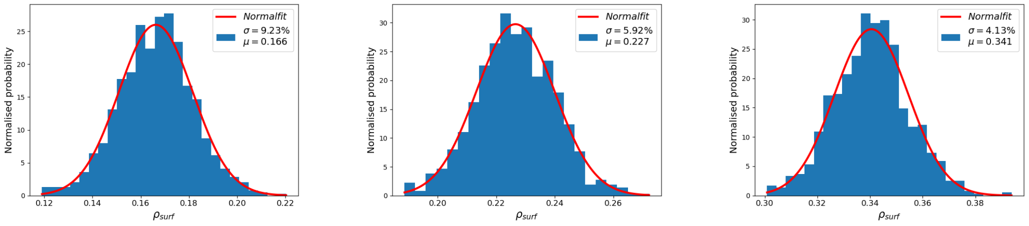

(a) B1 (b) B2 (c) B3

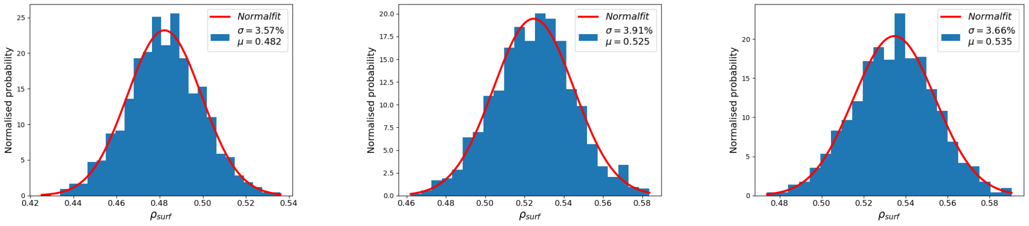

(d) B4 (e) B5 (f) B6

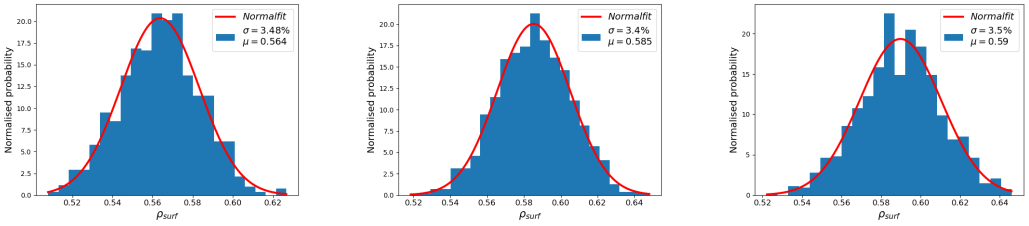

(g) B7 (h) B8 (i) B8A

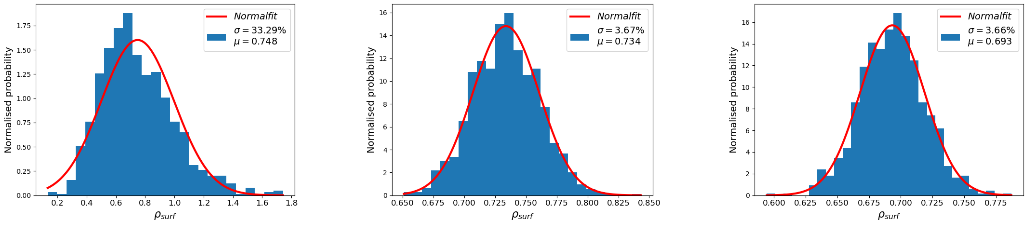

(j) B9 (k) B11 (l) B12

Figure B.22: Surface reflectance Libya4

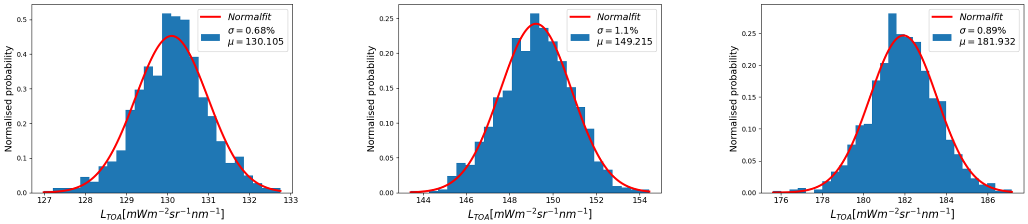

(a) B1 (b) B2 (c) B3

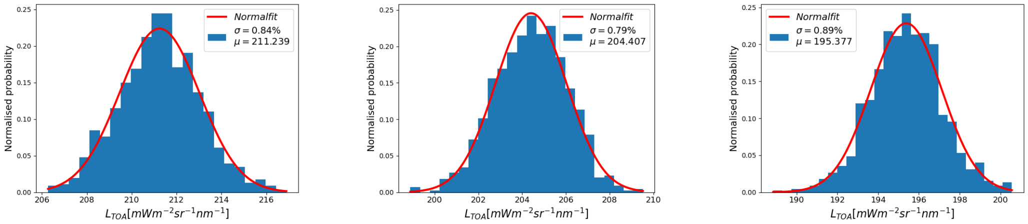

(d) B4 (e) B5 (f) B6

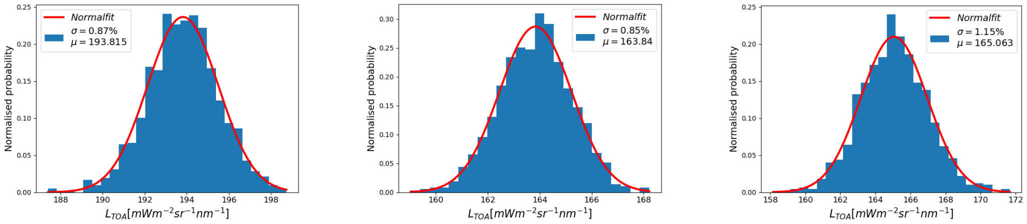

(g) B7 (h) B8 (i) B8A

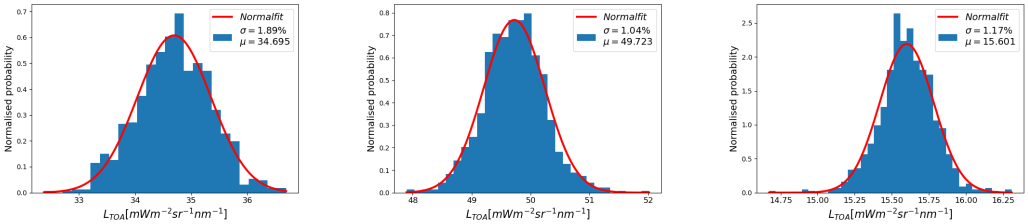

(j) B9 (k) B11 (l) B12

Figure B.23: TOA radiance Libya4

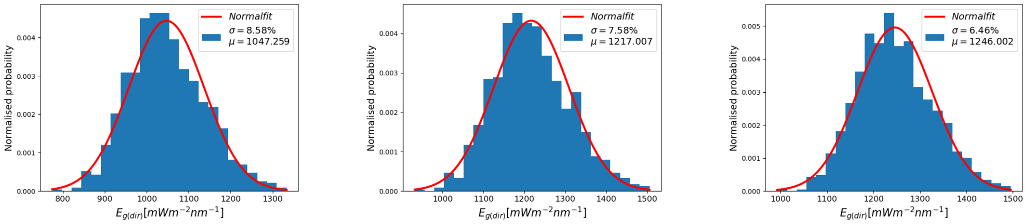

(a) B1 (b) B2 (c) B3

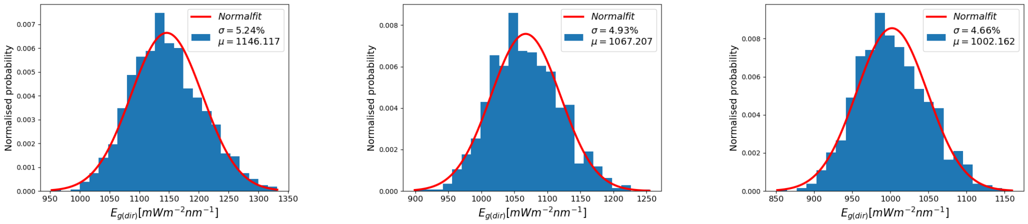

(d) B4 (e) B5 (f) B6

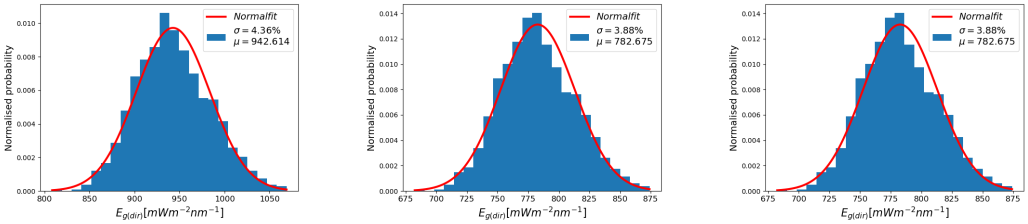

(g) B7 (h) B8 (i) B8A

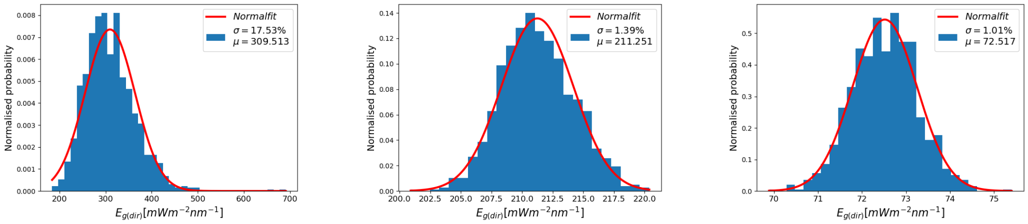

(j) B9 (k) B11 (l) B12

Figure B.24: Downwelling direct irradiance Libya4

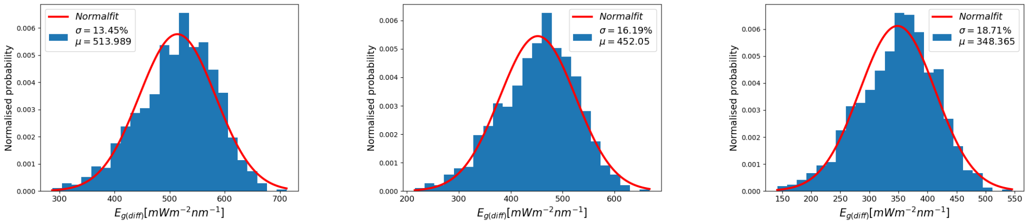

(a) B1 (b) B2 (c) B3

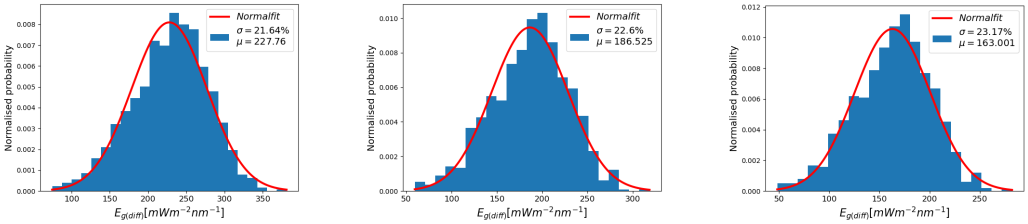

(d) B4 (e) B5 (f) B6

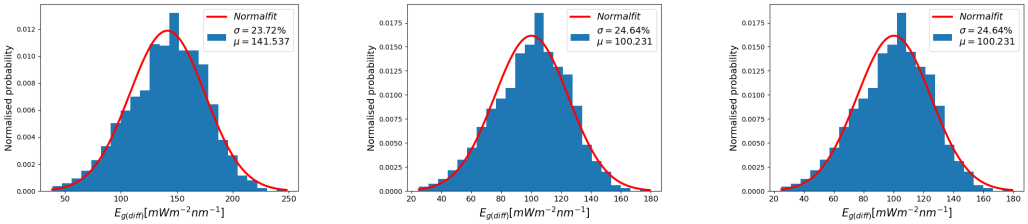

(g) B7 (h) B8 (i) B8A

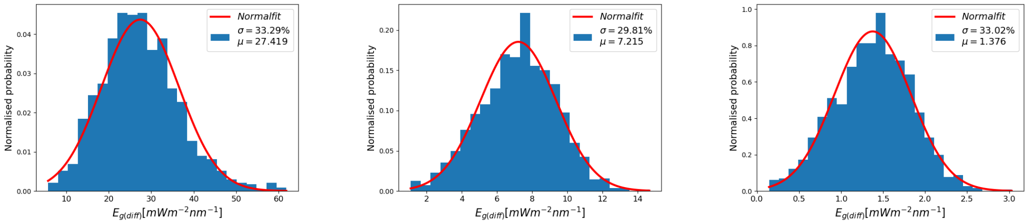

(j) B9 (k) B11 (l) B12

Figure B.25: Downwelling diffuse irradiance Libya4

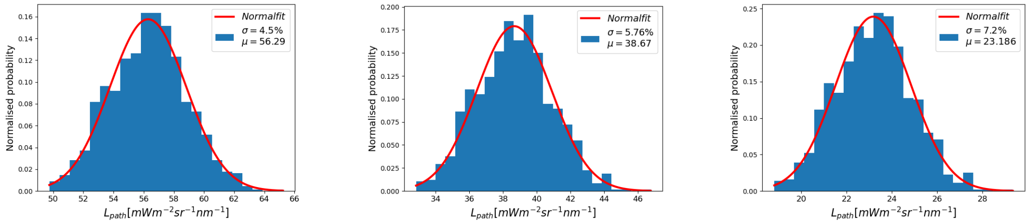

(a) B1 (b) B2 (c) B3

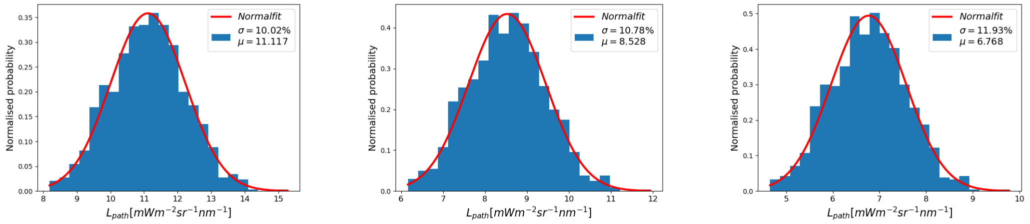

(d) B4 (e) B5 (f) B6

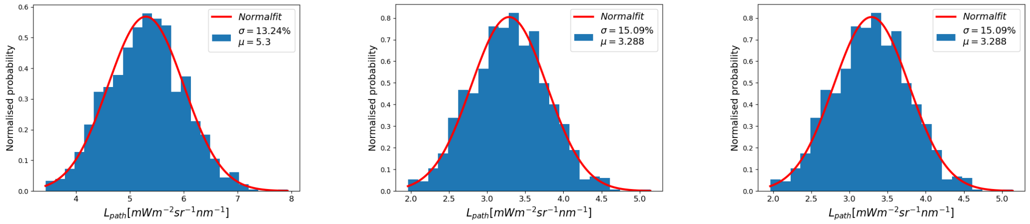

(g) B7 (h) B8 (i) B8A

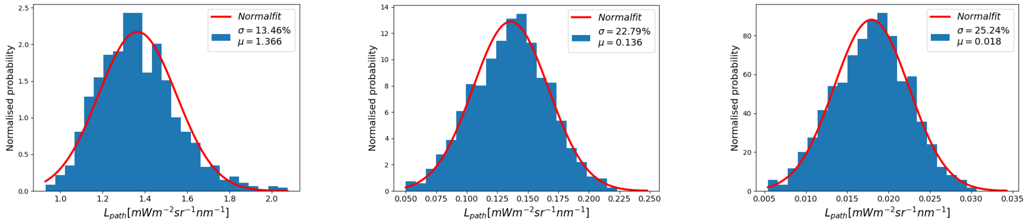

(j) B9 (k) B11 (l) B12

Figure B.26: Path radiance Libya4

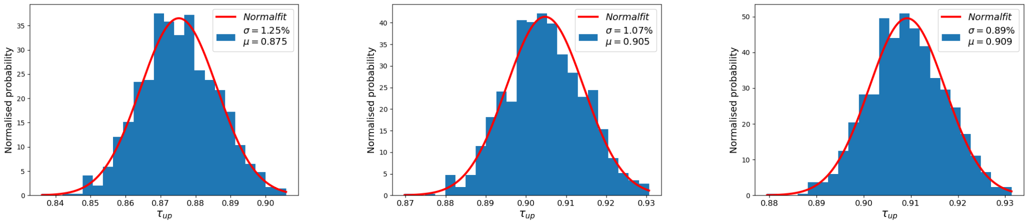

(a) B1 (b) B2 (c) B3

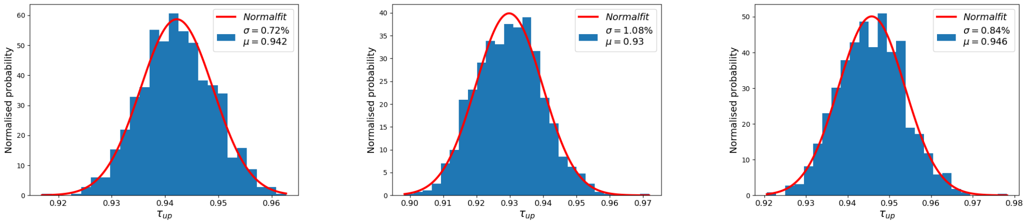

(d) B4 (e) B5 (f) B6

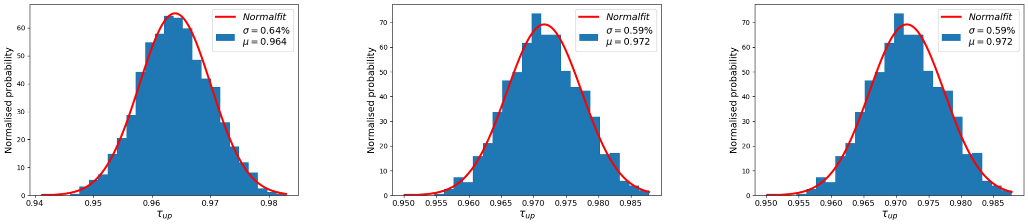

(g) B7 (h) B8 (i) B8A

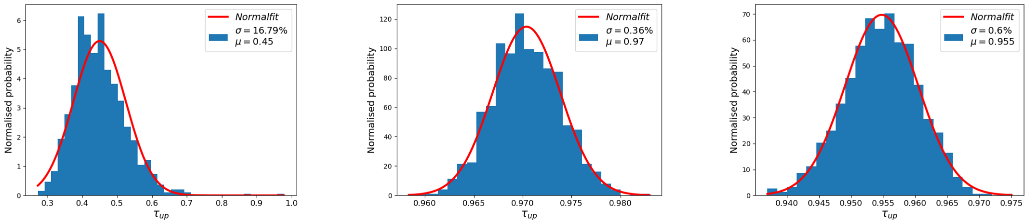

(j) B9 (k) B11 (l) B12

Figure B.27: Ground-to-TOA transmittance Libya4

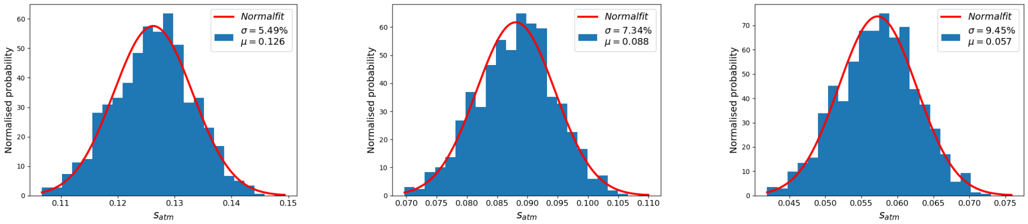

(a) B1 (b) B2 (c) B3

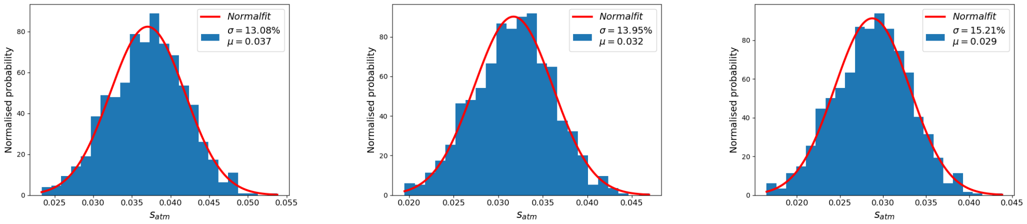

(d) B4 (e) B5 (f) B6

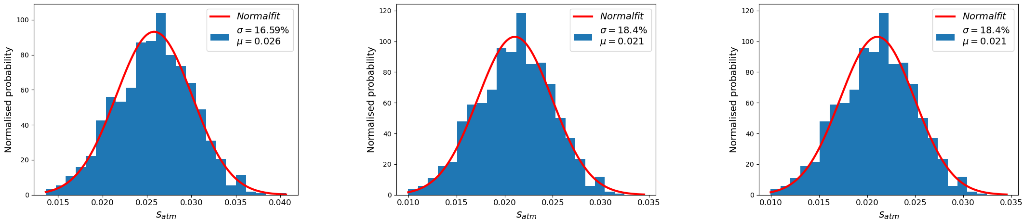

(g) B7 (h) B8 (i) B8A

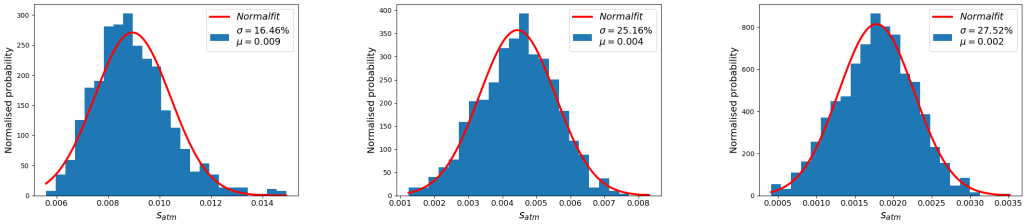

(j) B9 (k) B11 (l) B12

Figure B.28: Spherical albedo Libya4

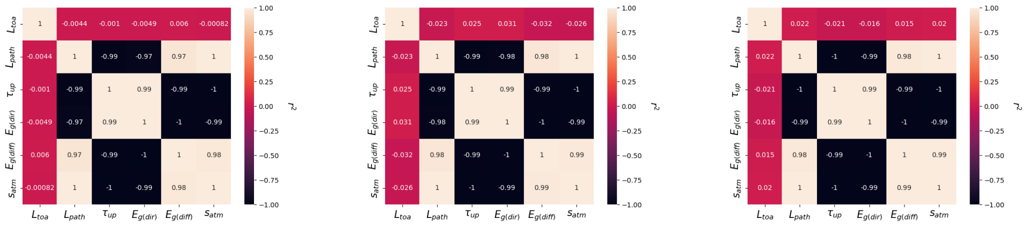

(a) B1 (b) B2 (c) B3

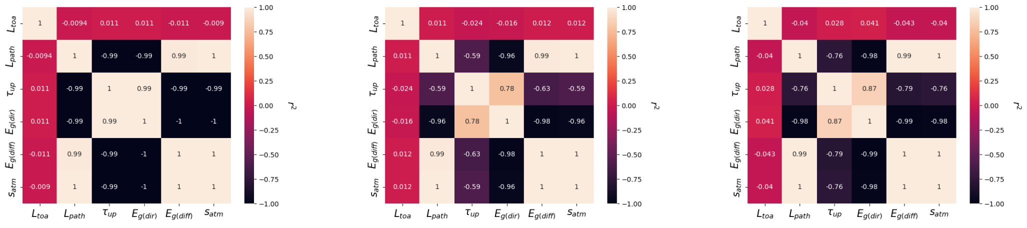

(d) B4 (e) B5 (f) B6

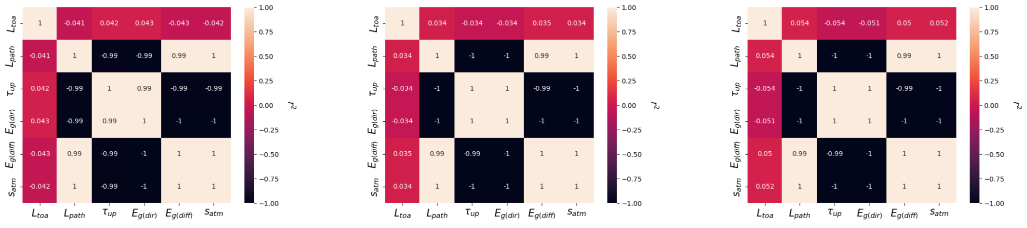

(g) B7 (h) B8 (i) B8A

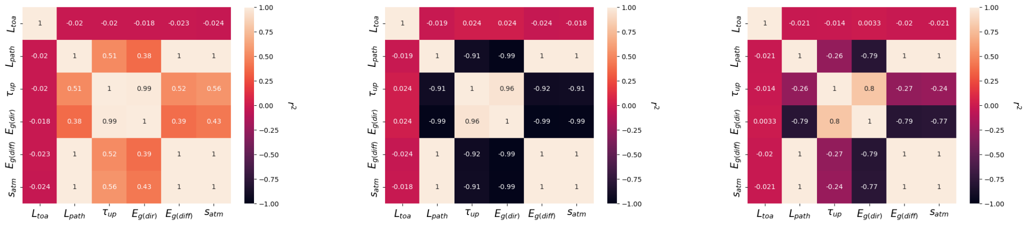

(j) B9 (k) B11 (l) B12

Figure B.29: Atmospheric function correlation Libya4

Appendix C. CURUC results

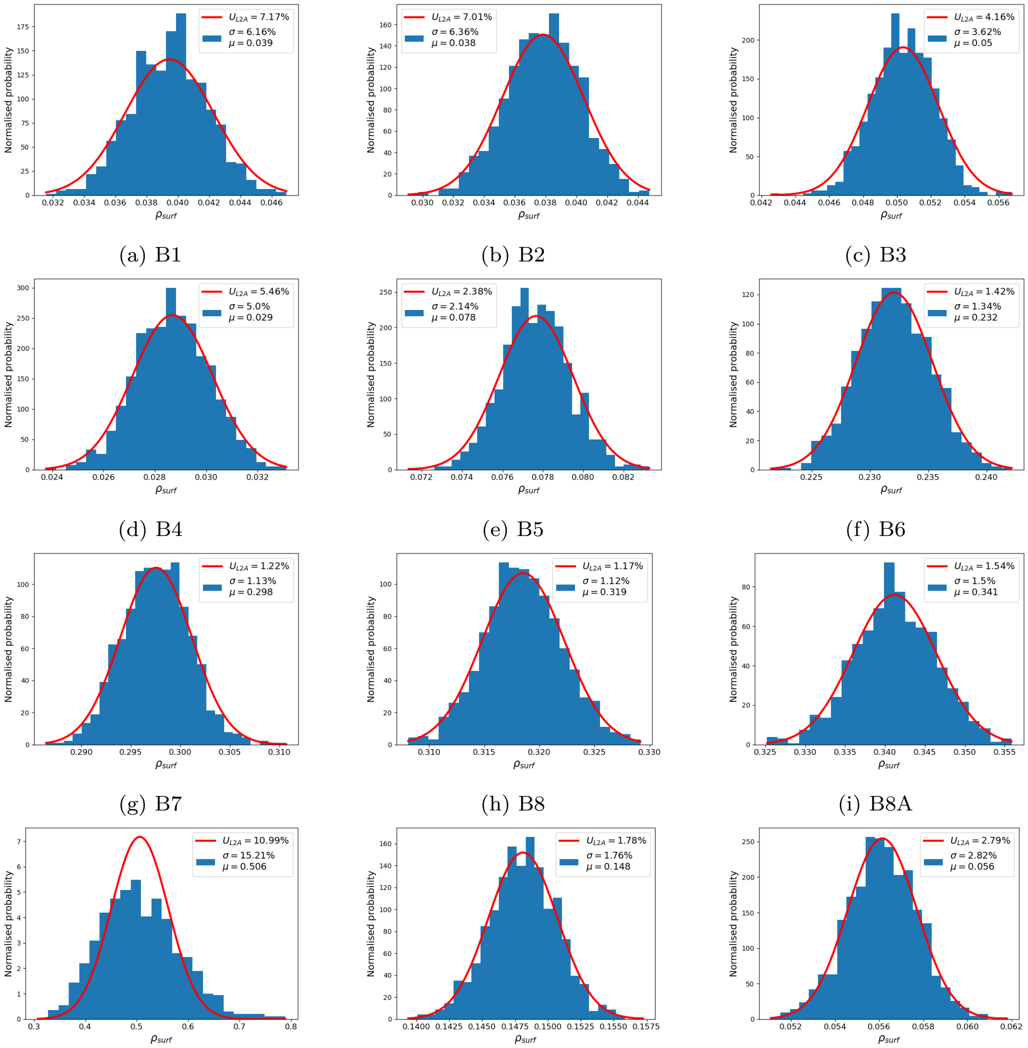

(a) B1 (b) B2 (c) B3

(d) B4 (e) B5 (f) B6

(g) B7 (h) B8 (i) B8A

(j) B9 (k) B11 (l) B12

Figure C.30: Surface reflectance in the Amazon case obtained for a uniform lambertian approach (i.e. equation 2 in subsection 2.2.5) for both the MCM mulitvariate and GUM analytical approach.

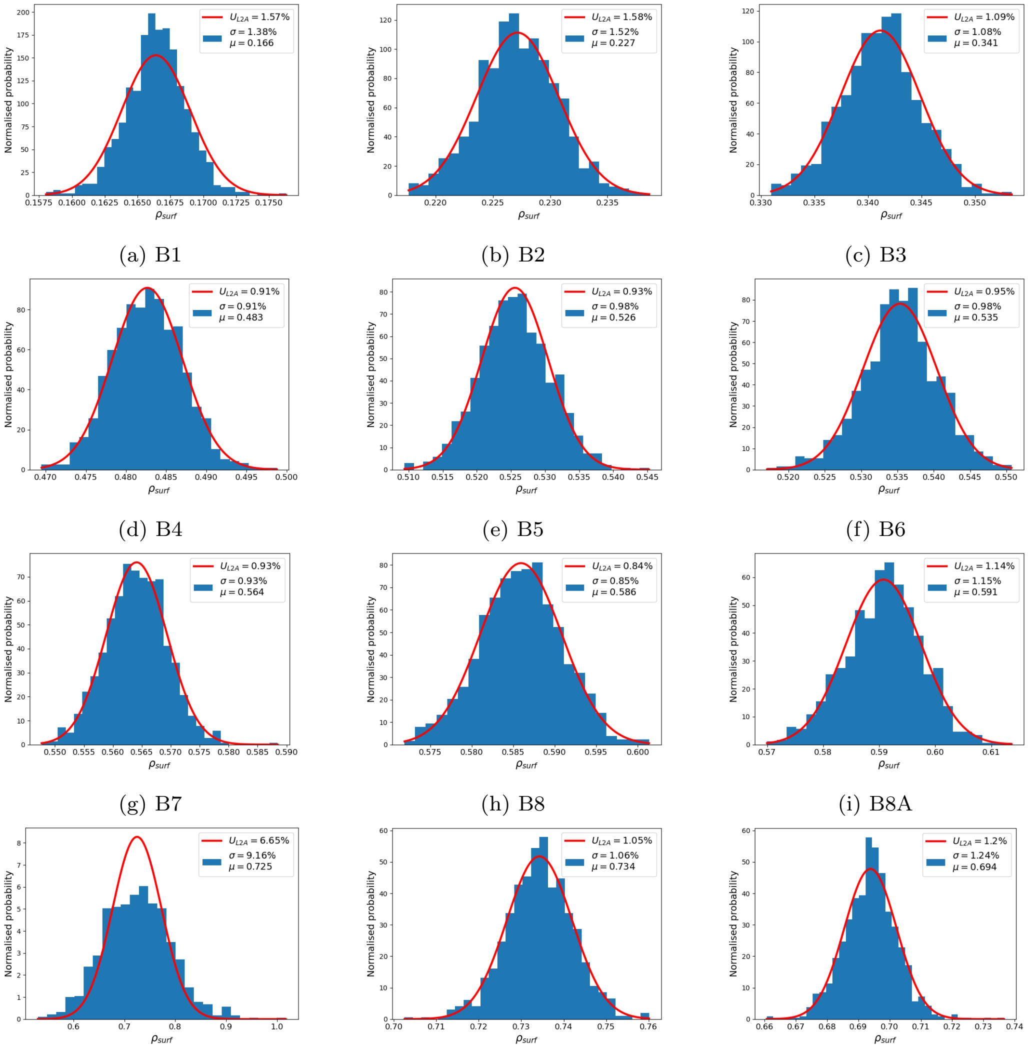

(a) B1 (b) B2 (c) B3

(d) B4 (e) B5 (f) B6

(g) B7 (h) B8 (i) B8A

(j) B9 (k) B11 (l) B12

Figure C.31: Surface reflectance in the Libya4 case obtained for a uniform lambertian approach (i.e. equation 2 in subsection 2.2.5) for both the MCM mulitvariate and GUM analytical approach.

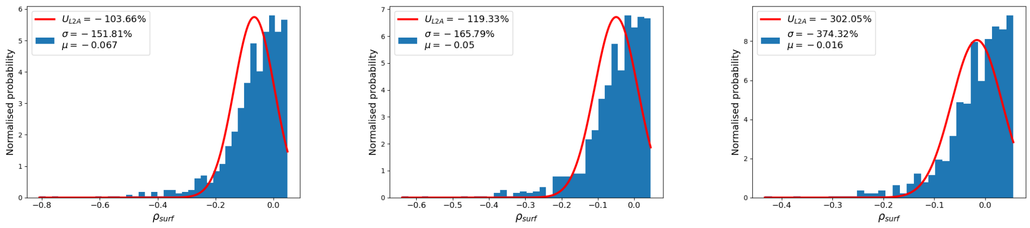

(a) B1 (b) B2 (c) B3

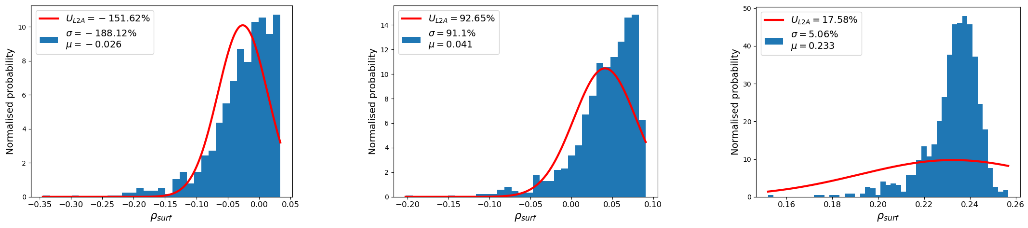

(d) B4 (e) B5 (f) B6

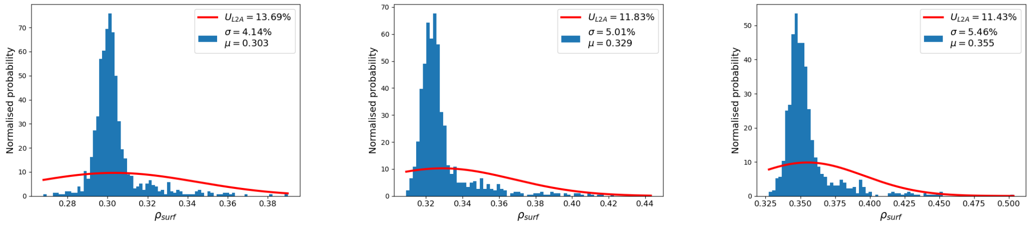

(g) B7 (h) B8 (i) B8A

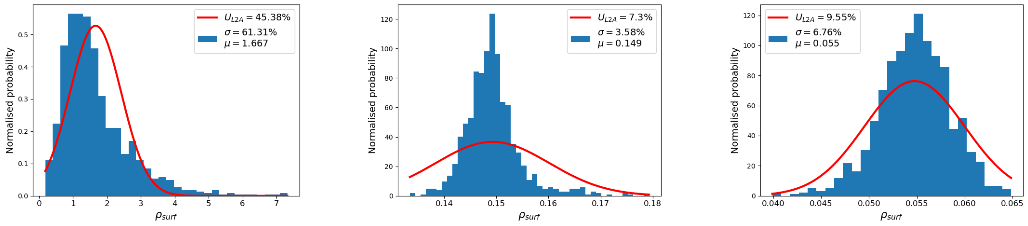

(j) B9 (k) B11 (l) B12

Figure C.32: Surface reflectance in the Amazon case obtained for a uniform lambertian approach (i.e. equation 2 in subsection 2.2.5) for both the MCM mulitvariate and GUM analytical approach. The simulation was forced to set a value of 5 cm for water vapour and 1.14 (approximately 5 km visibility) for AOT.

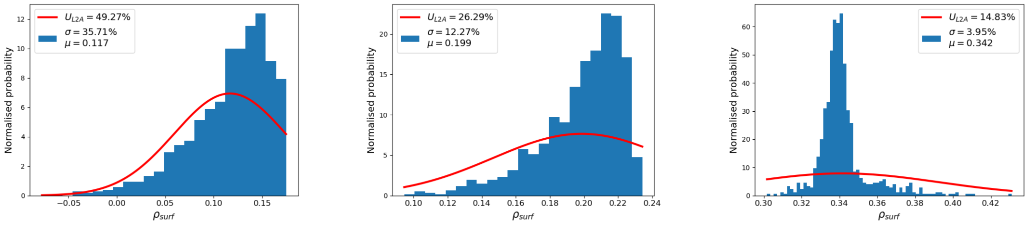

(a) B1 (b) B2 (c) B3

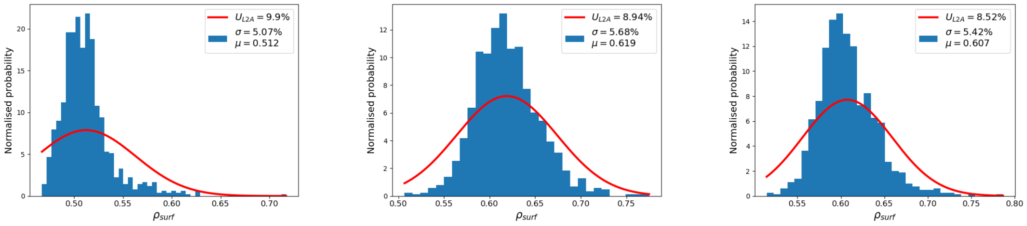

(d) B4 (e) B5 (f) B6

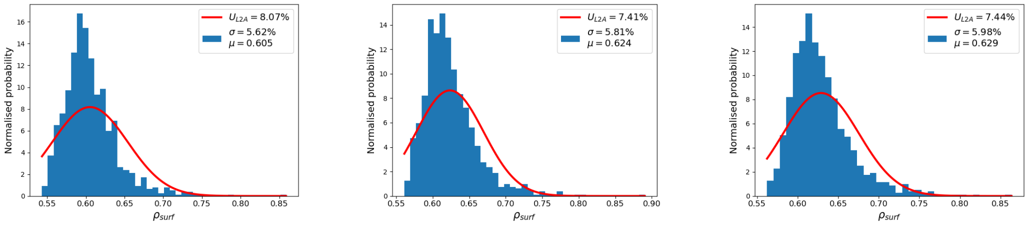

(g) B7 (h) B8 (i) B8A

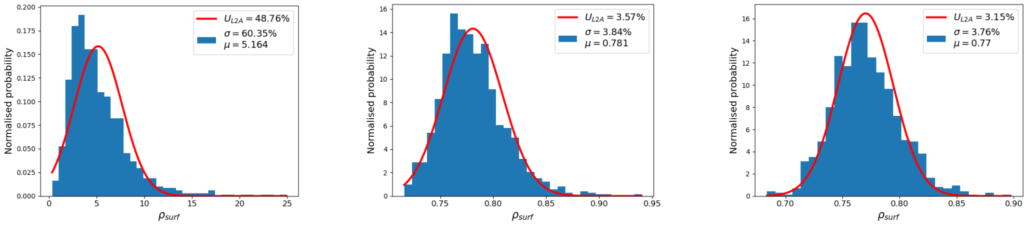

(j) B9 (k) B11 (l) B12

Figure C.33: Surface reflectance in the Libya4 case obtained for a uniform lambertian approach (i.e. equation 2 in subsection 2.2.5) for both the MCM mulitvariate and GUM analytical approach. The simulation was forced to set a value of 5 cm for water vapour and 1.14 (approximately 5 km visibility) for AOT.

Appendix D. Python script: *run_L2a_unc.py*

```python
from datetime import datetime
import numpy as np
import L2a_unc
import plots_L2aunc

samples = 1000
librad_bin = None # path to folder with libradtran binary. E.
                               g. '/home/gorrono/libRadtran-2
                               .0.4'
lut = L2a_unc.L2aUnc(librad_bin, samples)
case = 'user'  # 'user', 'libya4' , 'amazon', 'winterwheat'
                               or 'maize'
subcase = 'standard' # 'standard', 'curuc' and 'reptrantest'
                               options for cases 'libya4' and
                                'amazon'

if case == 'user':  # user defined case.
    path_l1c = None # FULLPATH_TO_L1C.zip'
    path_l2a = None # FULLPATH_TO_L2A.zip'
    latlon = (None, None) # LATITUDE AND LONGITUDE
    roisize = (None, None) # AREA SIZE IN METERS
    toairrad_flag = False
    adjacency_flag = True
    lambertian_flag = True
    libradunc_flag = True
    lut.get_libradunc(path_l1c, path_l2a, latlon, roisize,
                                   toairrad_flag,
                                   adjacency_flag,
                                   lambertian_flag,
                      libradunc_flag)
    lut.plot_results(toairrad_flag)
```

References

Braverman, A., Hobbs, J., Teixeira, J., Gunson, M., 2021. Post hoc uncertainty quantification for remote sensing observing systems. SIAM/ASA Journal on Uncertainty Quantification 9, 1064–1093. URL: https://doi.org/10.1137/19M1304283, doi:10.1137/19M1304283, arXiv:https://doi.org/10.1137/19M1304283.

Brodrick, P.G., Thompson, D.R., Fahlen, J.E., Eastwood, M.L., Sarture, C.M., Lundeen, S.R., Olson-Duvall, W., Carmon, N., Green, R.O., 2021. Generalized radiative transfer emulation for imaging spectroscopy reflectance retrievals. Remote Sensing of Environment 261, 112476. URL: https://www.sciencedirect.com/science/article/pii/S0034425721001942, doi:https://doi.org/10.1016/j.rse.2021.112476.

Cosnefroy, H., Leroy, M., Briottet, X., 1996. Selection and characterization of saharan and arabian desert sites for the calibration of optical satellite sensors. Remote Sensing of Environment 58, 101–114. URL: https://www.sciencedirect.com/science/article/pii/0034425795002111, doi:https://doi.org/10.1016/0034-4257(95)00211-1.

Cox, M.G., Siebert, B.R.L., 2006. The use of a Monte Carlo method for evaluating uncertainty and expanded uncertainty. Metrologia 43, S178–S188. URL: https://doi.org/10.1088/0026-1394/43/4/s03, doi:10.1088/0026-1394/43/4/S03. publisher: IOP Publishing.

Dragani, R., 2011. On the quality of the era-interim ozone reanalyses: comparisons with satellite data. Quarterly Journal of the Royal Meteorological Society 137, 1312–1326. URL: https://rmets.onlinelibrary.wiley.com/doi/abs/10.1002/qj.821, doi:https://doi.org/10.1002/qj.821, arXiv:https://rmets.onlinelibrary.wiley.com/doi/pdf/10.1002/qj.821.

Drusch, M., Del Bello, U., Carlier, S., Colin, O., Fernandez, V., Gascon, F., Hoersch, B., Isola, C., Laberinti, P., Martimort, P., Meygret, A., Spoto, F., Sy, O., Marchese, F., Bargellini, P., 2012. Sentinel-2: Esa's optical high-resolution mission for gmes operational services. Remote Sensing of Environment 120, 25–36. URL: https://www.sciencedirect.com/science/article/pii/S0034425712000636, doi:https://doi.org/

`10.1016/j.rse.2011.11.026`. the Sentinel Missions - New Opportunities for Science.

Emde, C., Buras-Schnell, R., Kylling, A., Mayer, B., Gasteiger, J., Hamann, U., Kylling, J., Richter, B., Pause, C., Dowling, T., Bugliaro, L., 2016. The libradtran software package for radiative transfer calculations (version 2.0.1). Geoscientific Model Development 9, 1647–1672. URL: `https://gmd.copernicus.org/articles/9/1647/2016/`, doi:`10.5194/gmd-9-1647-2016`.

Esposito, J.A., Xiong, X., Wu, A., Sun, J., Barnes, W.L., 2004. MODIS reflective solar bands uncertainty analysis, in: Barnes, W.L., Butler, J.J. (Eds.), Earth Observing Systems IX, International Society for Optics and Photonics. SPIE. pp. 448 – 458. URL: `https://doi.org/10.1117/12.558106`, doi:`10.1117/12.558106`.

Franch, B., Vermote, E., Sobrino, J., Fédèle, E., 2013. Analysis of directional effects on atmospheric correction. Remote Sensing of Environment 128, 276–288. URL: `https://www.sciencedirect.com/science/article/pii/S0034425712004063`, doi:`https://doi.org/10.1016/j.rse.2012.10.018`.

García-Haro, F.J., Campos-Taberner, M., Muñoz-Marí, J., Laparra, V., Camacho, F., Sánchez-Zapero, J., Camps-Valls, G., 2018. Derivation of global vegetation biophysical parameters from eumetsat polar system. ISPRS Journal of Photogrammetry and Remote Sensing 139, 57–74. URL: `https://www.sciencedirect.com/science/article/pii/S0924271618300625`, doi:`https://doi.org/10.1016/j.isprsjprs.2018.03.005`.

Gascon, F., Bouzinac, C., Thépaut, O., Jung, M., Francesconi, B., Louis, J., Lonjou, V., Lafrance, B., Massera, S., Gaudel-Vacaresse, A., et al., 2017. Copernicus sentinel-2a calibration and products validation status. Remote Sensing 9, 584. URL: `http://dx.doi.org/10.3390/rs9060584`, doi:`10.3390/rs9060584`.

Gasteiger, J., Emde, C., Mayer, B., Buras, R., Buehler, S., Lemke, O., 2014. Representative wavelengths absorption parameterization applied to satellite channels and spectral bands. Journal of Quantitative Spectroscopy and Radiative Transfer 148, 99–115. URL: `https://www.sciencedirect.`

com/science/article/pii/S0022407314002842, doi:https://doi.org/10.1016/j.jqsrt.2014.06.024.

Gorroño, J., Guanter, L., 2021. Assessing the radiometric impact of the Sentinel 2 orthorectification process, in: Babu, S.R., Hélière, A., Kimura, T. (Eds.), Sensors, Systems, and Next-Generation Satellites XXV, International Society for Optics and Photonics. SPIE. p. 118580W. URL: https://doi.org/10.1117/12.2603730, doi:10.1117/12.2603730.

Gorroño, J., 2023. gorronyo/s2-l2a-rut: First prototype version doi:10.5281/zenodo.7826096.

Gorroño, J., Fomferra, N., Peters, M., Gascon, F., Underwood, C.I., Fox, N.P., Kirches, G., Brockmann, C., 2017. A radiometric uncertainty tool for the sentinel 2 mission. Remote Sensing 9. URL: https://www.mdpi.com/2072-4292/9/2/178, doi:10.3390/rs9020178.

Gorroño, J., Hunt, S., Scanlon, T., Banks, A., Fox, N., Woolliams, E., Underwood, C., Gascon, F., Peters, M., Fomferra, N., Govaerts, Y., Lamquin, N., Bruniquel, V., 2018. Providing uncertainty estimates of the sentinel-2 top-of-atmosphere measurements for radiometric validation activities. European Journal of Remote Sensing 51, 650–666. doi:10.1080/22797254.2018.1471739.

Govaerts, Y., Nollet, Y., Leroy, V., 2022. Radiative transfer model comparison with satellite observations over ceos calibration site libya-4. Atmosphere 13. URL: https://www.mdpi.com/2073-4433/13/11/1759, doi:10.3390/atmos13111759.

Graf, L., Gorroño, J., Hueni, A., Walter, A., Aasen, H., 2023. Propagating Sentinel-2 Top-of-Atmosphere Radiometric Uncertainty into Land Surface Phenology Metrics Using a Monte Carlo Framework URL: https://www.techrxiv.org/articles/preprint/Propagating_Sentinel-2_Top-of-Atmosphere_Radiometric_Uncertainty_into_Land_Surface_Phenology_Metrics_Using_a_Monte_Carlo_Framework/22179673, doi:10.36227/techrxiv.22179673.v1.

Hu, B., Lucht, W., Strahler, A., 1999. The interrelationship of atmospheric correction of reflectances and surface brdf retrieval: a sensitivity study.

IEEE Transactions on Geoscience and Remote Sensing 37, 724–738. doi:`10.1109/36.752189`.

Huete, A., Didan, K., Miura, T., Rodriguez, E.P., Gao, X., Ferreira, L.G., . Overview of the radiometric and biophysical performance of the MODIS vegetation indices 83, 195–213. URL: `https://www.sciencedirect.com/science/article/pii/S0034425702000962`, doi:`10.1016/S0034-4257(02)00096-2`.

JCGM, 2008a. Evaluation of measurement data - Guide to the expression of uncertainty in measurement. Technical Report 100.

JCGM, 2008b. Evaluation of measurement data — Supplement 1 to the "Guide to the expression of uncertainty in measurement" — Propagation of distributions using a Monte Carlo method. Technical Report 101.

Kaminski, T., Pinty, B., Voßbeck, M., Lopatka, M., Gobron, N., Robustelli, M., 2017. Consistent retrieval of land surface radiation products from eo, including traceable uncertainty estimates. Biogeosciences 14, 2527–2541. URL: `https://bg.copernicus.org/articles/14/2527/2017/`, doi:`10.5194/bg-14-2527-2017`.

Kaufman, Y., Wald, A., Remer, L., Gao, B.C., Li, R.R., Flynn, L., 1997. The modis 2.1-/spl mu/m channel-correlation with visible reflectance for use in remote sensing of aerosol. IEEE Transactions on Geoscience and Remote Sensing 35, 1286–1298. doi:`10.1109/36.628795`.

Kotchenova, S.Y., Vermote, E.F., Levy, R., Lyapustin, A., 2008. Radiative transfer codes for atmospheric correction and aerosol retrieval: intercomparison study. Appl. Opt. 47, 2215–2226. URL: `https://opg.optica.org/ao/abstract.cfm?URI=ao-47-13-2215`, doi:`10.1364/AO.47.002215`.

Louis, J., 2021. Sentinel-2 level-2a algorithm theoretical basis document.

Louis, J., Debaecker, V., Pflug, B., Main-Knorn, M., Bieniarz, J., Mueller-Wilm, U., Cadau, E., Gascon, F., 2016. Sentinel-2 sen2cor: L2a processor for users, in: Ouwehand, L. (Ed.), ESA Living Planet Symposium 2016, Spacebooks Online. pp. 1–8. URL: `https://elib.dlr.de/107381/`.

Louis, J., Pflug, B., Main-Knorn, M., Debaecker, V., Mueller-Wilm, U., Gascon, F., 2018. Integration and assimilation of meteorological (ecmwf) aerosol estimates into sen2cor atmospheric correction, in: IGARSS 2018 - 2018 IEEE International Geoscience and Remote Sensing Symposium, pp. 1894–1897. doi:`10.1109/IGARSS.2018.8517562`.

Maahn, M., Turner, D.D., Löhnert, U., Posselt, D.J., Ebell, K., Mace, G.G., Comstock, J.M., 2020. Optimal estimation retrievals and their uncertainties: What every atmospheric scientist should know. Bulletin of the American Meteorological Society 101, E1512 – E1523. URL: `https://journals.ametsoc.org/view/journals/bams/101/9/bamsD190027.xml`, doi:`https://doi.org/10.1175/BAMS-D-19-0027.1`.

Mayer, B., Kylling, A., 2005. Technical note: The libradtran software package for radiative transfer calculations - description and examples of use. Atmospheric Chemistry and Physics 5, 1855–1877. URL: `https://acp.copernicus.org/articles/5/1855/2005/`, doi:`10.5194/acp-5-1855-2005`.

Nicodemus, F., Richmond, J., Hsia, J.J., Ginsberg, I., Limperis, T., 1977. Geometrical Considerations and Nomenclature for Reflectance. Technical Report October. National Bureau of Standards, U.S. Department of Commerce. Washington, DC.

Richter, R., Schläpfer, D., 2019. Atmospheric and topographic correction (atcor theoretical background document). DLR IB 1, 0564–03.

Rodgers, C.D., 2000. Inverse Methods for Atmospheric Sounding. WORLD SCIENTIFIC. URL: `https://www.worldscientific.com/doi/abs/10.1142/3171`, doi:`10.1142/3171`, `arXiv:https://www.worldscientific.com/doi/pdf/10.1142/3171`.

Rouse, J.W., Haas, R.H., Schell, J.A., Deering, D.W., others, . Monitoring vegetation systems in the great plains with ERTS 351, 309.

S2 MSI ESL team, 2023. Sentinel 2 l2a data quality report 57.

Schaepman-Strub, G., Schaepman, M.E., Painter, T.H., Dangel, S., Martonchik, J.V., 2006. Reflectance quantities in optical remote sensing-definitions and case studies. Remote Sensing of Environment 103, 27–42. doi:`10.1016/j.rse.2006.03.002`.

Schläpfer, D., Borel, C.C., Keller, J., Itten, K.I., 1998. Atmospheric precorrected differential absorption technique to retrieve columnar water vapor. Remote Sensing of Environment 65, 353–366. URL: `https://www.sciencedirect.com/science/article/pii/S0034425798000443`, doi:`https://doi.org/10.1016/S0034-4257(98)00044-3`.

Team, Q.T., 2010. A quality assurance framework for earth observation: Principles.

Thompson, D.R., Bohn, N., Braverman, A., Brodrick, P.G., Carmon, N., Eastwood, M.L., Fahlen, J.E., Green, R.O., Johnson, M.C., Roberts, D.A., Susiluoto, J., 2021. Scene invariants for quantifying radiative transfer uncertainty. Remote Sensing of Environment 260, 112432. URL: `https://www.sciencedirect.com/science/article/pii/S0034425721001504`, doi:`https://doi.org/10.1016/j.rse.2021.112432`.

Thuillier, G., Hersé, M., Labs, D., Foujols, T., Peetermans, W., Gillotay, D., Simon, P., Mandel, H., 2003. The solar spectral irradiance from 200 to 2400 nm as measured by the solspec spectrometer from the atlas and eureca missions. Solar Physics 214, 1–22. doi:`10.1023/A:1024048429145`.

Thuillier, G., Hersé, M., Simon, P., Labs, D., Mandel, H., Gillotay, D., Foujols, T., 1998. The visible solar spectral irradiance from 350 to 850 nm as measured by the solspec spectrometer during the atlas i mission. Solar Physics 177, 41–61. doi:`10.1023/A:1004953215589`.

Toulemont, A., Olivier, M., Clerc, S., Bellouard, R., Reina, F., Gascon, F., Luce, J.F., Mavrocordatos, C., Boccia, V., 2021. Copernicus Sentinel-2C/D Multi Spectral Instrument full field of view spectral characterization, in: Babu, S.R., Hélière, A., Kimura, T. (Eds.), Sensors, Systems, and Next-Generation Satellites XXV, International Society for Optics and Photonics. SPIE. pp. 162 – 171. URL: `https://doi.org/10.1117/12.2593729`.

Vermote, E., Tanré, D., Deuzé, J., Herman, M., Morcrette, J., Kotchenova, S., 2006. Second simulation of a satellite signal in the solar spectrum-vector (6sv). 6S User Guide Version 3, 1–55.

Vicent, J., Rivera-Caicedo, J.P., Verrelst, J., Muñoz-Marí, J., Sabater, N., Berthelot, B., Camps-Valls, G., Moreno, J., 2021. Systematic assessment of modtran emulators for atmospheric correction. IEEE Transactions on Geoscience and Remote Sensing , 1–17doi:10.1109/TGRS.2021.3071376.

Widlowski, J.L., 2015. Conformity testing of satellite-derived quantitative surface variables. Environmental Science & Policy 51, 149–169. doi:10.1016/j.envsci.2015.03.018.

Xiong, X., Angal, A., Barnes, W., Chen, H., Chiang, V., Geng, X., Li, Y., Twedt, K., Wang, Z., Wilson, T., Wu, A., 2017. Updates of MODIS on-orbit calibration uncertainty assessments, in: Butler, J.J., Xiong, X.J., Gu, X. (Eds.), Earth Observing Systems XXII, International Society for Optics and Photonics. SPIE. p. 104020M. URL: https://doi.org/10.1117/12.2276305, doi:10.1117/12.2276305.

Yin, F., Lewis, P.E., Gómez-Dans, J.L., 2022. Bayesian atmospheric correction over land: Sentinel-2/msi and landsat 8/oli. Geoscientific Model Development 15, 7933–7976. URL: https://gmd.copernicus.org/articles/15/7933/2022/, doi:10.5194/gmd-15-7933-2022.